Cement and Concrete Research 159 (2022) 106888

Contents lists available at ScienceDirect

Cement and Concrete Research

journal homepage: www.elsevier.com/locate/cemconres

Mitigating alkali-silica reaction through metakaolin-based internal conditioning: New insights into property evolution and mitigation mechanism

Dayou Luo, Arkabrata Sinha, Madhab Adhikari, Jianqiang Wei *

Department of Civil and Environmental Engineering, Francis College of Engineering, University of Massachusetts Lowell, Lowell, MA 01854, USA

ARTICLE INFO

Keywords:
Internal conditioning
Alkali-silica reaction (C)
Degradation (C)
Metakaolin (D)
Lithium compounds (D)

ABSTRACT

This study investigates the role of metakaolin-based internal conditioning (MIC) in mitigating alkali-silica reaction (ASR) by monitoring volume expansion, cracking, permeability, strength, and microstructure of mortar containing reactive aggregates. Comprehensive insights into the mitigation mechanisms were obtained by elucidating the silica dissolution of aggregate and property evaluations of ASR gels with varying compositions. Substantial decreases in ASR expansion and cracking density up to 80.2 % and 73.5 %, respectively, revealed the robust role of MIC in ASR suppression outperforming single uses of metakaolin or lithium. A synergistic effect in suppressing multiple prerequisites of ASR was observed from the co-existing MIC and lithium, which was explained by the complementary efficiency between lithium and aluminum in suppressing silica dissolution, 55.7 % lower water uptake and 87.3 % less swelling potential of ASR gel, as well as the conversion of expansive ASR (Q^3) gel into non-expansive C-S-H (Q^2) phase making it a promising approach in designing durable concrete.

1. Introduction

After being identified by Stanton in an investigation of damaged concrete structures carried out by the California Division of Highways in the early 1940s [1], alkali-silica reaction (ASR), a series of complex chemo-physical "virulent" reactions between the alkaline cement matrix and non-crystalline silica in reactive or even normal aggregates, has become a major degradation mechanism of concrete and one of the leading causes of premature structural deterioration [2]. Although the mechanisms are still not fully understood, ASR is commonly considered as a multiple-step process consisting of dissolution of silica from aggregates, formation of colloidal silica sol, gelation of the sol, and swelling of the formed ASR gels [3]. The swelling of ASR gels in the presence of internal and external moisture results in the development of internal stresses in stiff concrete, causing irreparable volume expansion, cracking in both aggregates and the hydrated cement matrix, and substantial damages in concrete. In addition to a significant decrease in mechanical strength and stiffness, the formation of cracks can increase the permeability of concrete, inducing more complex coupled degradation mechanisms, such as delayed ettringite formation [4], freeze-thaw damage [5], and steel corrosion [6], and hence resulting in shortened structure service-life and significant maintenance costs. Due to its internal attribute, significant destructiveness, and irreversibility, ASR is commonly referred to as "concrete cancer" [7], and its widespread occurrences have become a critical issue in maintaining the service life of concrete structures.

To address the challenges arising from ASR, a variety of mitigation strategies have been investigated, which can be divided into four categories: (i) use of non-reactive or low-reactive aggregates with less metastable silica; (ii) use of low-alkali cement; (iii) incorporation of supplementary cementitious materials (SCMs), such as fly ashes [8], slag [9], silica fume [10], ground clay brick [11], rice husk ashes [12] and metakaolin (MK) [13]; and (iv) addition of lithium admixtures such as lithium carbonate [14] and lithium nitrate [15]. As reactive aggregate containing metastable silica is the principal cause of ASR's occurrence, the use of non-reactive aggregates is one of the most desirable methods. However, from petrography and mineralogy aspects, the resources of truly non-reactive aggregates are not always abundant, and it is, therefore, not practical in most countries or regions by taking local availability and cost into account. Choosing the proper categories of cement, such as low-alkali cement, is another way to avoid severe ASR, and it is being required in some areas (e.g., California of the United

* Corresponding author at: Department of Civil and Environmental Engineering, University of Massachusetts Lowell, 1 University Avenue, Shah Hall 200, Lowell, MA 01854, USA.
E-mail address: Jianqiang_wei@uml.edu (J. Wei).

https://doi.org/10.1016/j.cemconres.2022.106888
Received 22 March 2022; Received in revised form 7 June 2022; Accepted 19 June 2022
Available online 28 June 2022

States) where high-reactive aggregates dominate. For concrete structures with high ASR risk, however, limiting cement's alkali content even controlling alkali content in SCMs and aggregates, is passive and cannot be the sole strategy [3].

Since the early research findings by McCoy and Caldwell in 1951 [16], lithium compounds have been one of the commonly used admixtures to mitigate ASR in both new and existing concrete structures. In previous investigations, a variety of ASR mitigation mechanisms have been proposed for lithium-based admixtures. According to McCoy and Caldwell [16], among the eight lithium compounds, lithium nitrate showed a significant result in limiting ASR at the most effective amount of lithium dosage, yielding a lithium to alkali ratio of 0.74. Lawrence and Vivian [17] proposed that lithium can decrease the dissolution rate of silica in an equation and might decrease the repulsive force between ASR gel particles or change the ASR gels to less expansive products. Dimond [18] provided more insights into the mechanisms that lithium nitrate does not increase the pH of the pore solution, lithium can be partially sorbed by newly formed cement hydration products, and the Li^+ remains in pore solution can suppress ASR. By experimentally investigating six possible ASR mitigating mechanisms of lithium nitrate, Tremblay et al. [19] got a conclusion that increased chemical stability of reactive silica or early formation of a protective coating similar to classic ASR gel can better explain the effectiveness of lithium nitrate against ASR than other mechanisms, such as pH reduction, formation of less expansive products, and remaining dissolved silica in solution without forming expansive gels. According to the findings of Leemann et al. [20], on the one hand, the solubility of silica in the pore solution has been decreased by 45.2 % in the presence of lithium (Li/[K + Na] molar ratio of 0.74); on the other hand, the formation of non-expansive ASR gel was promoted by lithium as the calcium in the reaction products could be preferentially replaced by lithium instead of sodium and potassium ions. In a recent study by Guo et al. [21], the preferred reaction between the dissolved silica and lithium, as well as the formation of Li—Si phase as a surface barrier for silica dissolution, which prohibits both ASR and the reaction between dissolved silica and calcium hydroxide (CH), was identified via an in-situ Pair Distribution Function (PDF) measurement. While there is currently no proper guidance on the use of lithium compounds in concrete, several state departments of transportation in the United States, like Delaware, New Mexico, South Dakota, Texas, and Wyoming, permit the use of lithium in their specifications [15]. The high cost and resource scarcity, however, are critical challenges impeding the application of lithium in concrete structures. Moreover, the negative impact on early-age hydration of cement, increased autogenous shrinkage [22], and uncertain long-term efficiency of lithium are also limitations that need to be addressed.

The use of SCMs is now a fashion in the concrete world as they can consume CH, which is one of the main products formed during the cement hydration, to form additional calcium-silicate-hydrates (C-S-H) [23], or aluminum-containing C-S-H (C-A-S-H) [24], decrease the pH value of pore solutions [25], and reduce the permeability of concrete [26] through pozzolanic reactions. Although extensive research works have been performed to support the role of SCMs in improving concrete properties and suppressing ASR, high volume SCMs can significantly impact the structural performance of concrete. Moreover, the local availability of high-quality SCMs, i.e., low alkali, low-calcium, and narrowly variable chemistry that is needed in ASR mitigation, is uncertain. In recent years, MK, a calcined clay mineral industrially produced by heating kaolin to a temperature between 650 °C and 800 °C [27], attracted more curiosity among the SCMs due to its proven high pozzolanic reactivity and the great potential in improving mechanical strength and durability of concrete. Comparing with other SCMs, MK has a higher content of aluminum, which has been proven an effective agent to suppress ASR [28]. The anhydrous aluminum-silicate of MK after calcination, which is mainly amorphous, function as a reactive pozzolan that can modify the structure of C-S-H, form a barrier around the reactive silica to slow down the dissolution rate, and decrease the pH of pore solution, making it an ideal additive to control ASR [29]. In one of the author's previous investigations [2], it was found that ASR-induced expansion can be suppressed from deleterious to unconscious level by partially replacing 10 % to 30 % cement with MK. As per Ramlochan et al. [30], 20 % cement replacement by MK can effectively reduce the concentrations of OH^-, K^+, and Na^+ in the pore solution of concrete. Walters and Jones [31] found that no expansion or deleterious surface appearance was observed by incorporating up to 25 % MK over 18 months.

In addition to the emerging pozzolanic reactivity, the unique water absorption capacity of MK makes it an ideal internal curing agent in concrete if being used in a pre-saturated condition. The disordered alumina-silicate layered structure [32] and ultra-fine particle sizes [33] of the MK play a vital role in absorbing a significant amount of water that can be gradually released at a later age to fuel the continuous hydration of cement and hence improve the degree of hydration and mechanical properties, densifying microstructure, and decreasing autogenous shrinkage [34]. Currently, super-absorbent polymer (SAP) [35] and lightweight aggregate (LWA) [36] are commonly used as internal curing agents in concrete. However, few investigations on internal curing based on SCMs, especially MK, have been conducted. The ASR-induced cracking and damage in concrete can be decreased in internal-cured concrete with pre-wetted LWA as an internal curing agent, attributing to the formation of a denser and less permeable microstructure triggered by enhanced cement hydration [37]. However, a symbiotic side-effect was also proposed [38] that ASR may not be fully mitigated by LWA-based internal curing due to the fact that conventional internal curing using LWA can increase the internal relative humidity (RH) of concrete, thereby facilitating the occurrence of ASR and expansion of ASR gels. Unlike LWA and SAP, which can only provide additional water physically, a “duplex” function is hypothesized from the saturated MK in the cement system, i.e., the integration of unique pozzolanic reactions and more uniform distribution of water induced by the nanoscale clay particles to enhance cement hydration and modify properties of the cementitious matrix. And this can be upgraded to a “triplex” function if the pre-saturated MK nanoparticles are incorporated into cement together with lithium nitrate so that ASR might be effectively mitigated in an inventive way.

This work aims to explore a new ASR suppression strategy by covering multiple ASR mitigating mechanisms, including pozzolanic reaction, enhanced cement hydration, and the incorporation of retarding elements, such as aluminum and lithium. To address the aforementioned challenges, a novel MK-based internal conditioning (MIC) technique triggered by pre-saturated MK with varying degrees of saturation (DOS) and its coupled incorporation with lithium nitrate are investigated. To obtain comprehensive elucidations of the ASR suppression efficiency and uncover the roles and mechanisms of the ingredients in mitigating ASR, the investigations were conducted at three levels: (i) ASR-induced evolutions in volume expansion, cracking, permeability, compressive strength, and microstructure of mortars containing highly reactive fine aggregates; (ii) dissolution behavior of silica from the reactive aggregates in concrete pore solutions with varying concentrations of aluminum and lithium; and (iii) structural evolution, moisture absorption and swelling behavior of synthetic ASR gels.

2. Materials and methods

2.1. Materials

Type I/II Portland cement in compliance with ASTM C150 [39] and AASHTO M85 [40] produced by Quikrete was used in this study. The PowerPozz MK was sourced from South Carolina with a specific density of 2.6 g/cm^3. The chemical and mineral compositions of cement and MK analyzed by X-ray fluoresce (XRF) and X-ray diffraction (XRD) are summarized in Table 1. It shows that the equivalent alkalis in the cement

Table 1
Chemical and mineralogical compositions of the cementing materials (wt%).

	MK	Cement	
CaO	0.071	62.7	
SiO_2	51.8	20.1	
Al_2O_3	42.2	4.8	
SO_3	0.11	3.5	
Fe_2O_3	4.15	3.2	
MgO	–	3.4	
K_2O	0.218	$Na_2O + 0.658K_2O$	0.60
TiO_2	1.1	C_3S	54
ZrO_2	0.088	C_2S	17
SrO	0.04	C_3A	7
Cl	0.046	C_4AF	10

were 0.60 %, and the content of silicate and aluminate phases (SiO_2 + Al_2O_3) in MK is higher than 94 wt%. The particle size distributions (PSD) of cement and MK measured by laser diffraction are shown in Fig. 1. The used cement exhibits a specific surface area, Sauter mean diameter, and De Brouckere mean diameter of 1.66 m^2/g, 3.61 μm, and 23.93 μm, respectively. Compared to the cement, MK had a smaller particle size of 3.79 μm and a higher specific surface area that is almost 1.8 times that of cement. The water absorption capacity of the MK was determined per ASTM D 281-12 [41] and averaged by trice tests, wherein a full saturation yielded a 61.31 % water uptake by mass.

Highly reactive polymictic sand from EI Paso, Texas, United States, consisting of granites, volcanics, quartzite, chert, quartz, silicon carbide, and calcium carbonate [2,42–44], with a relative density of 2.39 and a fineness modulus of 2.96, was used. Among the minerals of the sand, the main reactive phase is chert, which contains readily dissolved silica to induce ASR in concrete. The PSD of the sands used for the compressive strength test was determined by sieve analysis and shown in Fig. 2. For the mortar bar test, the reactive sand was sieved and remixed to the particle size distribution suggested by ASTM C1260 [45]. Reagent-grade lithium nitrate with a density of 2.38 g/cm^3 and purity of 99 % was used as a lithium source. Extra pure sodium hydroxide with a purity of 97 % was used for making the 1 N NaOH solution used in the mortar bar test. Reagent grade CH (>95 %), sodium hydroxide, potassium hydroxide (>97 %), lithium nitrate (>99 %), sodium aluminate (>99.9 %), and colloidal nano-silica solution with a concentration of 50 %, a particle size of 0.02 μm, and an average particle surface area of 180 m^2/g were used to prepare the synthetic ASR gels. The simulated pore solution was prepared by dissolving CH, sodium metasilicate, sodium aluminate, potassium hydroxide, potassium sulfate (99.2 %), and sodium hydroxide in deionized (DI) water. In addition, lithium nitrate (>99 %) and aluminum nitrate (>98 %) were used for preparing the lithium and aluminum-containing pore solutions, respectively.

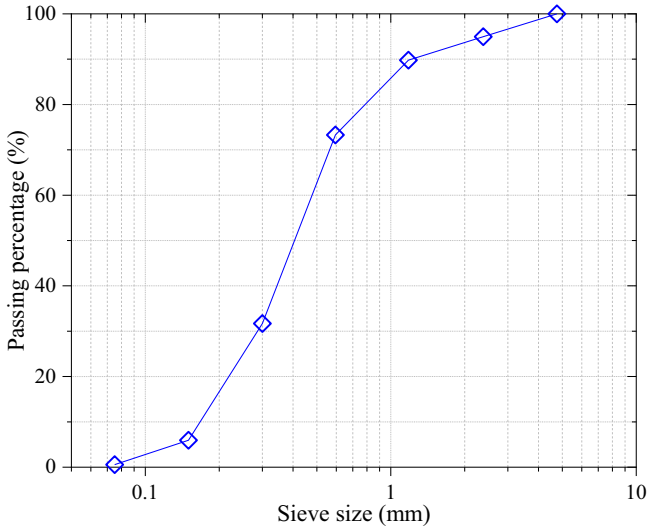

Fig. 2. Particle size distribution of the reactive sands used for bulk electrical resistivity and compressive strength tests.

2.2. Mixture proportion and specimen preparation

According to ASTM C1260 [45], mortars with a water to binder ratio (w/b) of 0.47 and a binder-to-sand ratio of 2.03 were used for the mortar bar test. The mix design is summarized in Table 2. To examine the roles of dry and wetted MK, lithium nitrate at different dosages, and the coupling effects of saturated MK and lithium in ASR mitigation, nine groups in total were prepared. Plain cement mixed with the reactive sand without incorporating MK and lithium was prepared as the control group. The "0.28Li" and "0.74Li" groups contain lithium nitrate at the lithium to alkali molar ratios of 0.28 and 0.74, respectively. All other groups are made from blended cement with 30 % cement replacement with MK. The "DMK" group was prepared via the conventional approach to incorporate 30 % dry MK. In contrast, 0.5MIC, 0.75MIC, and 1.0MIC containing 30 % pre-wetted MK with DOSs of 50 %, 75 %, and 100 % were cast to explore the benefits of MIC in ASR mitigation. Before mixing, the wetted MK samples at their certain DOSs were sealed for 12 h for moisture homogenization. For a comparison purpose, the

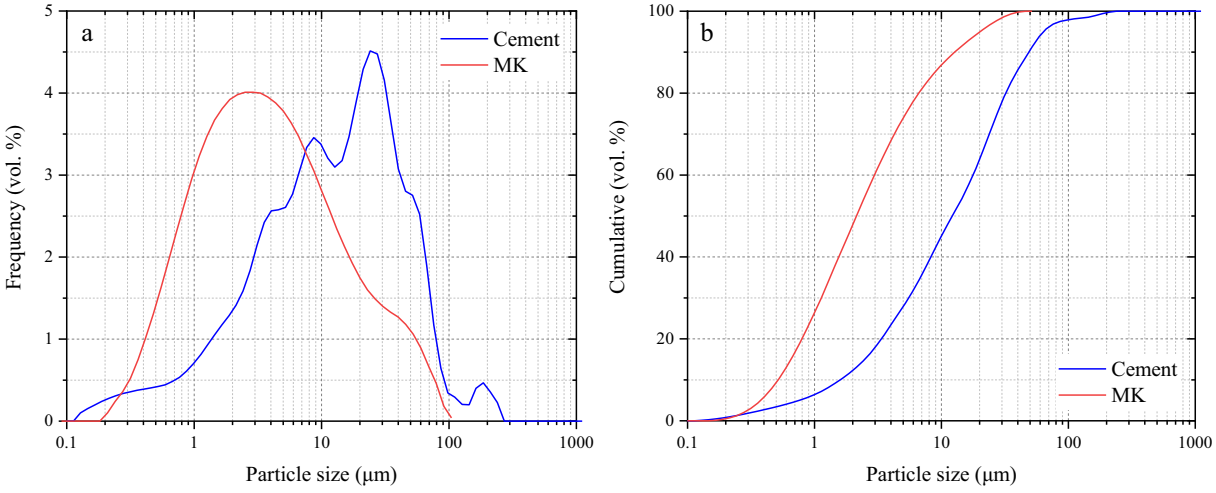

Fig. 1. Particle size distributions of the cement and MK determined by laser diffraction: (a) relative frequency of particles; (b) volume of the particles smaller than a certain diameter.

Table 2
The mixing proportion for the mortar bar test.

Index	Content (g)						w/b
	Cement	Water	$LiNO_3$	MK	Pre-wetted water	Sand	
PC	440	206.8	–	–	–	893	0.47
0.28Li	440	206.8	1.65	–	–	893	0.47
0.74Li	440	206.8	4.35	–	–	893	0.47
DMK	308	206.8	–	132	–	893	0.47
DMKEW	308	287.3	–	132	–	893	0.65
0.5MIC	308	206.8	–	132	40.21	893	0.47
0.75MIC	308	206.8	–	132	60.43	893	0.47
1.0MIC	308	206.8	–	132	80.25	893	0.47
LiMIC	308	206.8	3.05	132	80.25	893	0.47

"DMKEW" group was prepared by mixing 30 % dry MK plus extra mixing water, which yields the same amounts of MK and water as the "1.0MIC" group but in two different water supply strategies. Furthermore, a group with coupled incorporation of 0.74 lithium and 30 % fully saturated MK (LiMIC) was prepared to explore the potential coupling effect between MK-based internal curing and lithium (as-proposed MIC) on ASR mitigation. For each group, the cement binders were mixed with water and fine reactive aggregate using a mechanical mortar mixer and then cast in 25 mm × 25 mm × 280 mm stainless steel molds with pre-embedded studs making a 250 mm effective testing length. Two repetitions for each group with a total of 18 samples were prepared.

Except for 0.28Li, the other eight mixture proportions were employed for casting 50 mm × 50 mm × 50 mm cubic samples for compressive strength test at a w/b ratio of 0.4 and a binder-to-sand ratio of 1:1. Additionally, with the same mixing proportions, five groups, namely PC, 0.74Li, DMK, 1.0MIC, and LiMIC, were cast into 75 mm × 150 mm cylinder specimens to evaluate the ASR resistance of the mortars by means of electrical resistivity and permeability. After casting, all the specimens were covered with plastic sheets to keep moisture at 23.0 ± 2 °C for 24 h until demolding, further conditioning, or testing.

Two groups of reactive sand in different sizes (size 1: 300–600 μm; size 2: <150 μm) were immersed in the simulated cement pore solutions with various concentrations of Li or Al to evaluate the silica dissolution rate. Based on the real pore solution extracted from cement paste at 69 days according to [46], a simulated concrete pore solution with a pH value of 13.5 ± 0.1 was synthesized with the elemental concentrations of potassium, sodium, calcium, silicon, and aluminum at 493.63 mmol/L, 44.93 mmol/L, 2.44 mmol/L, 0.15 mmol/L, and 0.09 mmol/L, respectively. The solutions with lithium were prepared based on the same elemental concentrations by adding lithium nitrate at Li/[K + Na] ratios of 0.5, 0.75, and 1.0. As reported by [47], the aluminum concentration of a cement matrix containing 15 % MK can reach a maximum value of 2.73 mmol/L. In this study, by considering the different degrees of reaction of the 30 % MK, three aluminum concentrations of 2.73 mmol/L, 6.4 mmol/L, 10.0 mmol/L were employed to evaluate the role of aluminum played in silica dissolution. The elemental concentrations of the simulated cement pore solutions are summarized in Table 3.

To elucidate the ASR mitigation mechanisms, synthetic ASR gels with the mixing proportions as summarized in Table 4 were investigated. Based on 100 ASR gels collected from filed concretes, it was reported that the characteristic Ca/Si, K/Si, and Na/Si molar ratios of ASR gels are typically within the ranges of 0.05–0.5, 0.0–0.3, and 0.1–1.0 [48], respectively. Therefore, a control ASR gel group with the Ca/Si, K/Si, and Na/Si ratios of 0.5, 0.2, and 0.8, respectively, was synthesized. The ASR gel with lithium was prepared based on the control group by adding lithium nitrate at a Li/[K + Na] ratio of 0.3, while the one with aluminum was obtained by incorporating sodium aluminate with an Al/Si ratio of 0.3. In this group, the sodium in sodium aluminate was considered to keep the Na/Si ratio of 0.8. Another ASR gel sample was prepared by adding both lithium nitrate and sodium aluminate with the Li/[K + Na] and Al/Si ratios of 0.3 to examine the coupled lithium and aluminum on ASR gel properties. The raw materials in solid and liquid states were cooled at −20 °C and 1 °C, respectively, for at least 3 h. Then, the cooled alkali chemicals were pre-mixed in DI water to avoid rapid heat generation, agglomeration, and corrosive reaction, followed by the additions of CH and colloidal silica solution. All the chemical components were homogeneously mixed in a kitchen mixer. 25 mm × 25 mm × 25 mm cubic specimens were prepared and cured in a sealed condition for chemical analysis. XRD, thermogravimetric analysis (TGA), attenuated total reflectance–Fourier transform infrared (ATR-FTIR) spectroscopy, and dynamic vapor sorption (DVS) tests were conducted on ASR gel take from the core of the cubic specimens.

Table 3
The elemental concentrations for the simulated pore solutions.

Simulated pore solutions	Concentration (mmol/L)					Li/[K + Na] ratio
	K	Na	Ca	Si	Al	
Control	493.63	44.93	2.44	0.15	0.09	0
0.50Li	493.63	44.93	2.44	0.15	0.09	0.50
0.75Li	493.63	44.93	2.44	0.15	0.09	0.75
1.00Li	493.63	44.93	2.44	0.15	0.09	1.00
2.73Al	493.63	44.93	2.44	0.15	2.73	0
6.40Al	493.63	44.93	2.44	0.15	6.40	0
10.0Al	493.63	44.93	2.44	0.15	10.0	0

2.3. ASR expansion

ASTM C1260 [45] was followed to determine the expansion behavior of mortars due to ASR. After being demolded, the specimens were immersed in tap water at 23.0 ± 2 °C then conditioned at 80 °C in a mechanical oven for 24 h and the initial mortar bar length was measured as zero reading. Then, the mortar bar samples were immersed in a 1 N NaOH solution in sealed boxes at 80.0 ± 2 °C. The subsequent comparator readings were conducted after 12 and 24 h for the first day, once a day for the first week, and then two readings per week up to 80 days.

2.4. Cracking analysis

After 80 days of immersion in a 1 N NaOH solution at 80.0 ± 2 °C, two levels of microstructural analysis of the mortar bars were performed to obtain a comprehensive understanding of MIC on ASR-induced crack propagation in mortars. Firstly, the surface cracking behavior of the mortar bars was evaluated by a digital microscope, which was then quantified based on a grayscale method with an image processing program in ImageJ and MATLAB [49,50]. The cracks and background were distinguished by transforming the original images into binary images. After removing pixel noises and surface defects with a filter function in-built in ImageJ, the crack area and the maximum and average crack width were quantified based on the identified pixels and structs. As shown in Eq. 1, the cracking density (ρ_c) was calculated by dividing the crack area (A_c) by the selected surface area of the mortar bar (A_t).

$$\rho_c = \frac{A_c}{A_t} \times 100\% \quad (1)$$

Then, the cross-section of the selected mortar bars was investigated on polished surfaces using a JEOL JSM 7410F FE-SEM/EDS under an

Table 4
The mixing proportion for the synthetic ASR gels.

ASR gels	Ca/Si	K/Si	Na/Si	Li/[K + Na]	Al/Si
Control	0.5	0.2	0.8	0	0
Li	0.5	0.2	0.8	0.3	0
Al	0.5	0.2	0.8	0	0.3
Li + Al	0.5	0.2	0.8	0.3	0.3

accelerating voltage of 10.0 kV. A precise low-speed saw was used to cut the specimens into thin disks with a thickness of <2 mm. The sample was coated with gold film using a vacuum sputter coater (Denton Vacuum Desk IV). The formation of ASR gel and micro-cracks on the aggregates and the surrounding cement pastes were examined. The elemental quantification of the ASR gels and cement pastes was collected through an EDS Genesis XM2 imaging system composed of a 10 mm^2 Si (Li) detector with a SUTW window under an accelerating voltage of 5.0 kV.

2.5. Bulk electrical resistivity

The bulk electrical resistivity of cylindrical mortar samples was measured by the uniaxial method per ASTM C1876 [51] using a Giatec RCON2™ bulk resistivity tester (Giatec Scientific Inc., Ottawa, Canada). The method has been modified to investigate the effects of MK and lithium on ASR-induced microstructure evolution and permeability in mortars containing reactive aggregates. After demolding, the ends of the cylinders were polished using a handheld polisher and then cured in saturated lime water for 7 days at 23.0 ± 2 °C to obtain sufficient cement hydration and microstructure development. Subsequently, the specimens were transferred to a 1 N NaOH solution in sealed buckets at 23.0 ± 2 °C until testing at 28 days, 60 days, 90 days, 120 days, and 150 days. The results were obtained by averaging two repetitions.

The formation factor (FF) that is mainly used to describe the microstructure of saturated porous materials and related to transport properties of concrete is defined as the ratio of the bulk electrical resistivity of concrete (ρ_c, Ω·m) and the pore solution resistivity (ρ_s, Ω·m) [52] as shown in Eq. 2. The evolutions of bulk electrical resistivity and formation factor with time were fitted via an extended Freundlich equation (Eq. 3):

$$FF = \rho_c/\rho_s \tag{2}$$

$$y = ax^{bx^{-c}} \tag{3}$$

where a, b, and c are the fitting parameters.

2.6. Compressive strength

The development of mechanical property of the cement composites impacted by ASR was monitored in terms of compressive strength after 28 days, 60 days, and 90 days. The cubic specimens were cured under the same condition and procedure as the electrical resistivity test, and three repetitions for each group per testing age were tested using a CONTROLS automatic concrete compression machine at a loading rate of 900 N/s. The maximum load for each specimen was recorded, and the average value of each group was calculated as the representative strength. Moreover, the same groups, prepared with normal unreactive sands with a w/b ratio of 0.35, were cast and treated in saturated lime water at 23 ± 2 °C, the corresponding compressive strength was tested after 1 day, 7 days, and 28 days.

2.7. Silica dissolution of the reactive aggregates

10.0 ± 0.005 g of reactive sand in specific sizes (sand-1: <150 μm; sand-2: 300–600 μm) were washed 3 times with DI water to remove impurities and then oven-dried at 110 °C. After being cooled down to the room temperature, the dry sands were immersed in 250 mL simulated pore solutions, sealed in plastic bottles, and stored at room temperature (23 ± 2 °C) followed by shaking twice a day to avoid agglomeration. 2.5 mL of the solutions were withdrawn after 10 min, 1, 6, 24, 168, 336, and 672 h and diluted by a factor of 25 with 2 % nitric acid to stabilize the solution, then filtered through 0.22 μm syringe filters. The evolution of silicon concentration in the simulated pore solutions was analyzed by inductively coupled plasma-optical emission spectrometry (ICP-OES) by considering the volume change of the solutions after the sample collection at each testing age. The correlation between the dissolved silicon concentrations and the dissolving time up to 336 h was then fitted via the modified Weibull cumulative distribution function (CDF) [53]:

$$y = y_0 + A_1\left(1 - e^{-(x/a)^b}\right) \tag{4}$$

where y_0, A_1, a, and b are fitting parameters.

2.8. ASR gels characterization

After 28 days of reaction, the TGA of the ASR gels was carried out with a Perkin Elmer TGA 4000 thermogravimetric analyzer. A heating rate of 15 °C/min from 30 °C to 900 °C under N_2 purge gas at a flow rate of 20 mL/min was applied. The XRD investigation was performed with an AXRD powder X-ray diffractometer at 30 kV and 20 mA. After 28 days and 180 days of reaction, the ASR gels were scanned on rotary support in stepwise mode with a step size of 0.02° (2θ) and a scanning time of 5 s per step. ATR-FTIR spectroscopy was performed on the synthetic ASR gels after 28 days and 180 days using a Thermo Fisher Scientific Nicolet iS10 FTIR spectrometer. The spectra between 2000 cm^{-1} and 400 cm^{-1} were acquired by the co-addition of 128 scans with a resolution of 4 cm^{-1}.

Both the static moisture absorption behavior at a constant RH and dynamic absorption behavior under varying RH of the ASR gels were investigated based on ATR-FTIR and DVS, respectively. After 120 days of reaction, the ASR gels were dried for 48 h at 23 ± 2 °C in a vacuumed desiccator, equipped with sodium hydroxide solution to maintain a 9 % RH and soda-lime to minimize carbonation. Then, around 1 g of the dry ASR gels from each group was measured by ATR-FTIR within a spectra range between 4000 cm^{-1} and 1500 cm^{-1}. The rest of the samples were transferred to a sealed container with an equilibrium RH of 97 % maintained by a saturated potassium sulfate solution, and the ATR-FTIR measurements in the same spectra range (4000 cm^{-1} to 1500 cm^{-1}) were conducted periodically for up to 48 h to understand the static moisture absorption behavior of the ASR gels. The dynamic moisture sorption behavior of the ASR gels was monitored with a DVS Intrinsic II system (Surface Measurement System LTD, PA) under stepped RH between 0 % and 95 % at 25 °C. Around 20 mg of ASR gels were used for each test. In the drying process, the RH was first set equal to 95 %, then decreased to 90 %, followed by RH decrease to 0 % with a 10 % decrement. Upon mass equilibrium at the end of drying, the wetting process was started to investigate the moisture absorption of the ASR gels based on an inverse RH increase to 95 % with the same step size intervals. Mass, temperature, and humidity data for each RH step were recorded for 24 h with a 1 min time interval. Equilibrium was considered to be reached when the mass change rate is <0.0015 %/min over 10 min.

A modified standard protocol of ASTM C1608 [54] for the determination of hydraulic cement chemical shrinkage was followed to monitor the shrinkage and swelling behavior of the ASR gels. About 15 mL synthetic homogeneously mixed ASR gels were cast in ∅31.25 mm by 78.00 mm cylinder vials and covered by paraffin oil. The cylinder vials were tightly sealed with rubber stoppers equipped with 2 mL capillary tubes with an accuracy of 0.0025 mL in the center. The volume changes of the ASR gels were monitored by reading the height of paraffin oil in the graduated capillary tubes. 32 holes with a diameter of 0.15 mm were drilled around the vial containers at the bottom, where ASR gels were cast to avoid leakage of paraffin oil and ensure that the ASR gels were exposed to the simulated cement pore solution as needed. The holes were sealed with two layers of water-proof tape during the first 42 days to ensure sufficient reaction, then the tapes were removed, and the lower part of the vial container was immersed in a simulated cement pore solution (the control group in Table 3) with 2 repetitions of each group to measure the swelling behavior of the ASR gels in the presence of pore solution. The whole test was conducted at a temperature of 23 ± 2 °C.

The first reading was taken after the gels' initial setting (e.g., 2 days after casting for the control gel and 5 days for the groups with lithium and lithium plus aluminum due to the retarded reaction and hardening). The volume change of the ASR gels during the 42 days of the sealed curing process and the free swelling behavior in the presence of cement pore solution up to 120 days were monitored based on periodically recording of the paraffin oil levels in the capillary tubes. For the swelling period, the volume at 42 days was set as the initial reading.

3. Results and discussion

3.1. ASR expansion

The volume expansion of mortars induced by ASR was measured for 80 days through a standard mortar bar test per ASTM C 1260 [45], which states an expansion of <0.1 % at 16 days after casting (or 14 days' immersion in a 1 N NaOH solution) is indicative of innocuous behavior, and an expansion >0.2 % is an indication of potentially deleterious behavior of the reactive aggregates presenting in the cement matrix. From Fig. 3a, the control group exhibited a high increase rate at an early age with a volume expansion exceeding 0.2 % within only 2 days, which is in the range of deleterious expansion defined in the standard [45]. After being immersed in the 1 N NaOH solution for 14 days and 80 days, this control group yielded an expansion of 0.70 % and 1.2 %, respectively, indicating the high reactivity of the chert-containing fine aggregate used here and the urgency of ASR mitigation.

Although similar trend as the control group was still observed from the groups with lithium, the ASR-induced expansion was decreased by 0.28Li and 0.74 Li. This volume expansion suppression might be due to the decreased dissolution rate of silica, which dominates the overall rate of ASR in concrete [20]. At the beginning of ASR, OH^- ions attack the siloxane groups on the reactive aggregate surface and break them down to form silanol groups. In the presence of lithium, silanol groups immediately react with Li^+ and Ca^{2+} ions present in the pore solution to form reaction products of lithium silicate, which acts as a physical barrier that covers the surface of the reactive aggregate to prevent further attacks of reactive silica by OH^- ions [55]. Moreover, from a previous study [15], lithium can alter the structure of ASR gel, probably helping to reduce the water absorption of ASR gel and make it non-expansive. Although 0.74Li was found to be the least effective dosage in previous studies [15,56], the ASR mitigation efficiency of the lithium-based admixtures depends on the reactivity of aggregates [57]. As shown in Fig. 3a, the 14-day expansion of the 0.74Li group is still at the deleterious level. In addition, it is noted that the expansion suppression efficiency of lithium nitrate decreased over time. It should be noted that, in the accelerated ASR test of this study, the continuous immersion of the mortar bars in the 1 N NaOH solution makes it hard to maintain the Li/[K + Na] ratio in the specimens over time, which might negatively impact the long-term ASR mitigation efficiency of lithium. This explains the decreased slopes of the volume expansion curves obtained from 0.28Li and 0.74Li during the first 10 days, while their later-age expansion rate (the slopes after 10 days) are comparable to the control group. This might also occur for some real cases of ASR-affected concrete structures exposed to external alkali resources or water (solution). These observations indicate that, for concrete containing highly reactive aggregates, ASR mitigation cannot fully rely on the use of lithium admixtures (at least in the presence of alkali solutions) even at the recommended dosage.

In contrast with lithium, the ASR-induced expansion was more drastically decreased by replacing 30 % of cement with dry MK, the 14-day expansion of which is lower than the 0.1 % innocuous criterion. Compared with the control group, the expansion of DMK was decreased by 77.9 % after 80 days of immersion. Interestingly, the 80 days expansion of the DMK group is 73.9 % lower than that of 0.74Li, which means MK itself can suppress ASR in concrete, outperforming lithium admixtures due to 1) its high amorphous silicate and aluminate contents and the consequent high pozzolanic activity, 2) the reduced permeability of the concrete (see Section 3.3), and 3) the altered hygroscopicity and swelling potential of ASR gels (see Section 3.6.3). These results reveal the effective ASR mitigation of the incorporated MK and agree well with the observations reported in previous studies [2,58], wherein the high ASR mitigation potential of MK was identified at cement substitution levels between 5 % and 30 %. It was observed that, although ASR-induced expansion can be significantly suppressed, the expansion of the DMK group exhibited an almost constant increasing rate with time during the entire testing period.

As shown in Fig. 3b, the incorporations of saturated MK with varying DOSs showed slightly less-effective ASR mitigation than the DMK group, especially during the first 30 days. Due to the sensitivity of ASR to moisture, a slight positive correlation was observed between the expansion of the mortars and the DOS of the incorporated MK. This correlation was also found from the group containing DMK plus the same amount of free water equivalent to the 1.0MIC with an expansion of 0.093 % after 14 days, which is 86.7 % lower than the control group but 151.4 % higher than the group with DMK only. After 17 days of immersion in 1 N NaOH solutions, the three pre-saturated MK groups

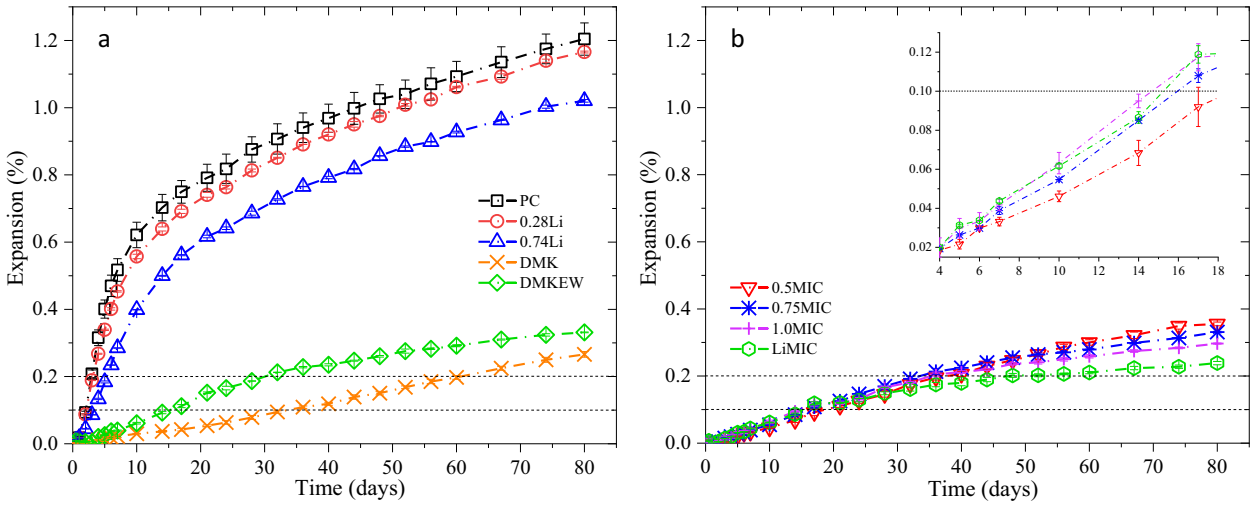

Fig. 3. ASR-induced volume expansion of mortar bar specimens and thresholds according to ASTM C1260: (a) lithium nitrate and DMK and (b) coupling effect of pre-saturated MK and lithium nitrate.

exhibited lower expansion than the group with DMKEW until the end of the test, except for the 0.5MIC group that showed a slightly higher expansion after 56 days. It should be noted that, although the ASR expansion mitigating efficiency of the pre-wetted MK exhibited a positive correlation with the DOS at an early age (up to 50 days), the long-term expansion decreased with the DOS of MK. After 80 days of immersion, the groups with 0.5MIC, 0.75MIC, and 1.0MIC expanded by 0.355 %, 0.331 %, and 0.297 %, respectively. This suggests the benefit of the gradually released water from the saturated MK in enhancing the efficiency of MK in mitigating ASR. This positive role of the MIC can also be identified from the comparison between the groups containing 1.0MIC and DMKEW. Although the two groups contain the same total amount of water, the simple addition of extra water provided more free water instead of gradually released water to impact the strength development of the cement composites. More importantly, this extra free water can directly fuel the ASR gel's swelling, which eventually results in the volume expansion of the mortar. As a result, the DMKEW group exceeds the deleterious line (0.2 %) after 30 days, while the groups with fully saturated MK exceed this expansion value 6 days later.

It was interestingly observed that the development of ASR-induced expansion of the groups containing partially and fully saturated MK exhibited an inflection point right after exceeding the 0.2 % line. As a result, after 80 days of immersion, the expansions of the groups with 0.5MIC, 0.75MIC, and 1.0MIC were lower than the control group, but higher than the DMK group. Although the expansion test was stopped at 80 days, based on the slope of the expansion curves, it can be anticipated that an expansion lower than that of the DMK group can be obtained from the groups with saturated MK, especially the one with 1.0MIC, at a later date. This again indicates that the MIC, which gradually releases water from the absorbent (MK) to the cement matrix fueling the continuous cement hydration and enhancing the pozzolanic reaction from MK, is an effective approach to mitigate long-term ASR deterioration in concrete.

Most interestingly, the ternary cement blend incorporated with 30 % fully saturated MK (1.0MIC) and 0.74Li shared the same expansion curve with the 1.0MIC during the first 21 days of immersion, while a lower expansion was yielded from the LiMIC group with a divergence increasing over time. With coupled incorporation of 0.74Li and 1.0MIC, the deleterious line (0.2 %) was exceeded after 48 days, which is 46 days and 16 days later than the control and 1.0MIC, respectively. Moreover, the expansion curve of this ternary group exhibited a lower increasing slope after exceeding the 0.2 % threshold, and its expansion hence became lower than that of the DMK group from 67 days. This indicates that adding 0.74Li could compensate for the increased ASR expansion by the extra water provided by the pre-saturated MK making it a robust strategy to mitigate ASR expansion. This suggested the synergistic effect of lithium nitrate and MIC, especially for the benefit of long-term ASR mitigation.

3.2. Cracking behavior

After 80 days of immersion in the 1 N NaOH solution at 80 °C, the surface cracking behavior of the mortar specimens was detected. From Fig. 4a and b, cracking can be clearly identified on the surface of the control group with more cracks and larger crack size than the group with 0.28Li (Fig. 4c) and 0.74Li (Fig. 4d). No visible cracks can be observed on the specimen surfaces of the groups containing 30 % MK, either dry (DMK and DMKEW) or pre-saturated (MIC), and only microcracks can be detected under a microscope. It is a clear indication that MIC plays a more effective role than lithium in mitigating ASR, which agrees well with the mitigated expansion behavior (Fig. 3). To obtain a comprehensive understanding of the ASR-induced surface cracking of the

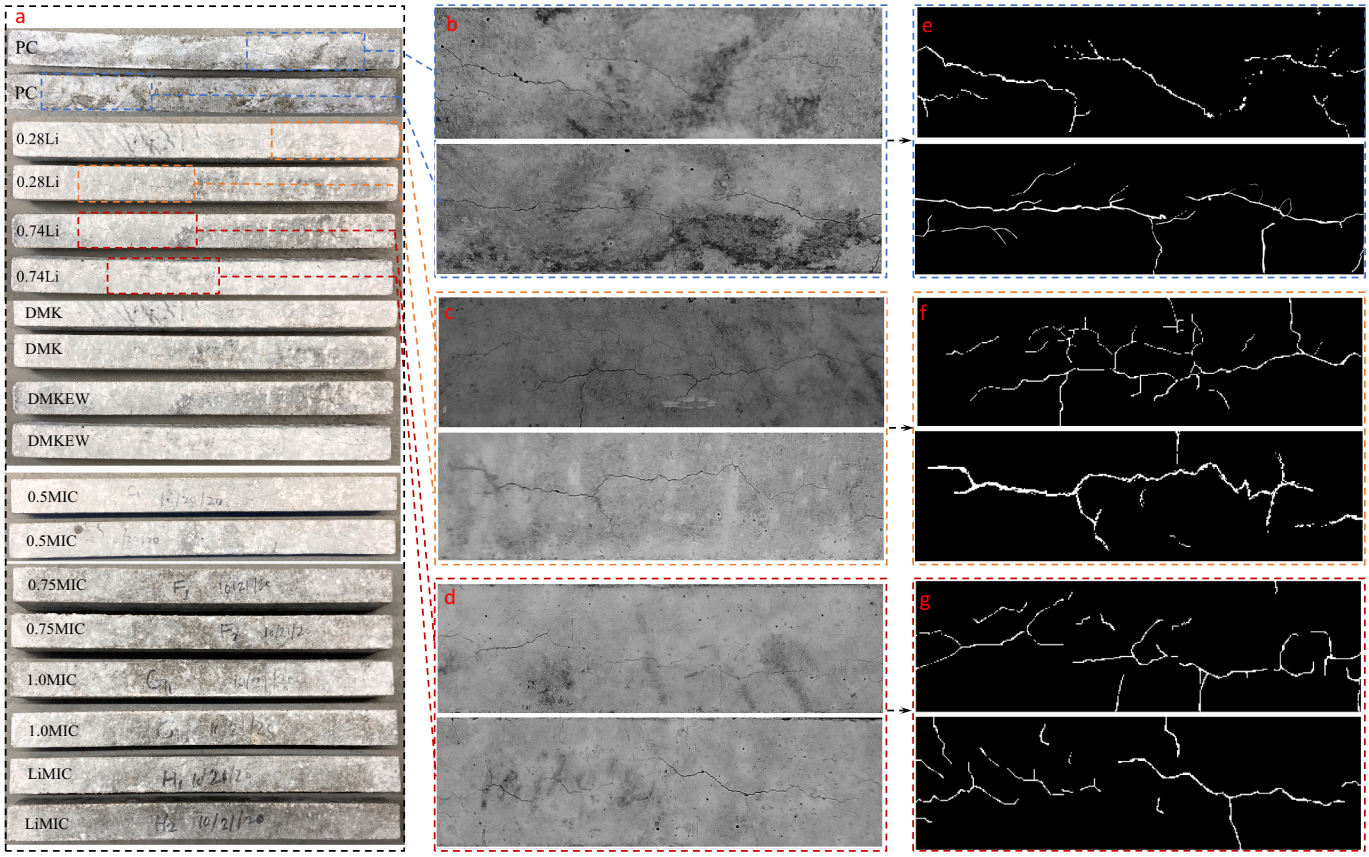

Fig. 4. Visual inspection of surface cracking of the mortar bar specimens immersed in 1 N NaOH solution at 80 °C for 80 days: (a) comparison of all groups, (b) PC, (c) 0.28Li, (d) 0.74Li, and filtered images of (e) PC, (f) 0.28Li and (g) 0.74Li.

mortar specimens and quantification of the role of MIC in suppressing ASR, the maximum and average crack with, as well as cracking density, were determined via a digital image processing toolbox based on the integration of ImageJ and MATLAB (see Fig. 4e to g).

The correlations between the maximum and average crack width and that between crack density and the ASR-induced expansion of the mortar bars after 80 days of immersion in 1 N NaOH are presented in Fig. 5a and b, respectively. From Fig. 5a, a positive linear correlation between the average crack width and maximum crack width could be apparently identified. The highest average crack width and maximum crack width were yielded from the control group, showing the values of 257.9 μm and 473.9 μm, respectively. Compared with the control group, 0.28Li and 0.74Li showed 17.6 % and 30.4 % lower average crack width, respectively, while the maximum crack width was decreased by 12.4 % and 33.5 %. A more pronounced crack width decrease was observed from the groups containing MK, with the average and maximum crack widths falling in the ranges of 25–55 μm and 50–115 μm, respectively. The average and maximum crack widths of DMK are 10.7 % and 11.0 % of the control group. However, both the average and maximum crack widths were increased by the extra water in either MIC or DMKEW groups. DMKEW and 1.0MIC yielded 85.5 % and 4.6 % higher average crack widths than DMK. It should be noted that lower crack widths were obtained by pre-saturating the MK (1.0MIC) than simply adding extra mixing water (DMKEW), indicating that MIC can compensate for the negative effect in crack width evolution. Further decreases in average and maximum crack widths were monitored from the LiMIC group, presenting 2.8 % and 5.9 % lower than that of the 1.0MIC, which again revealed the synergistic effect of lithium and MIC.

As seen in Fig. 5b, a positive correlation between the ASR-induced expansion and the crack density of the mortar bars satisfactorily fitted by a Gaussian function ($R^2 > 0.91$) was observed from the group except for 1.0MIC and LiMIC. The highest expansion of 1.2 % from the control group resulted in the highest cracking density of 3.7 %. In the presences of 0.28Li and 0.74Li, the cracking density was decreased by 18.9 % and 27.0 %. A dramatic drop of the crack density was observed from the groups containing MK with varying DOS. The DMK showed a crack density of 1.7 %, while a higher crack density was observed from 0.5MIC (1.8 %) and 0.75MIC (2.0 %). Agreeing with the observations in average and maximum crack widths, the DMKEW group presented a crack density of 1.9 % higher than that of DMK and 0.5MIC. This indicates the superiority of MIC outperforming a simple increase in mixing water, and an appropriate DOS of MK is required to maximize the role of MIC in mitigating ASR-induced deteriorations. When the DOS reaches 100 % (1.0MIC), a further decrease in cracking density was yielded. Agreeing well with all the findings above, the coupled lithium and MIC (LiMIC) yielded the lowest cracking density of 0.98 % along with the most mitigated ASR expansion. As a result, the data of 1.0MIC and LiMIC drift from the Gaussian fitting curve revealed the more substantial mitigation of cracking even with slight differences in ASR expansion.

3.3. Bulk electrical resistivity

The ASR-induced cracking can substantially impact the transport properties of concrete by providing paths for external moisture and aggregates salts. It is well known that the transport of ions, such as Cl^-, SO_4^{2-}, OH^- and alkalis ions, through the concrete in the microstructural scale can negatively impact concrete durability by inducing a variety of deteriorations, including chloride corrosion, sulfate attack, ASR, etc. [59]. Therefore, electrical resistivity was widely used as an indicator of concrete durability [60]. The transport properties of concrete can be reversely evaluated by electrical resistance, where the concrete is connected with two electrodes to evaluate the transportation of free electrons or charged ions within the matrix of the concrete. Therefore, a higher bulk electrical resistivity is an indication of lower permeability as a result of a denser microstructure [61]. Typically, the electrical resistivity of the concrete is controlled by multiple factors, including moisture content [62], ions' motion [63], ions' concentration [64], pore structure, and connectivity [62]. The ASR expansion and the consequent cracking can result in a significant increase in permeability of the concrete, thereby exhibiting decreased electrical resistance. By taking this into account, in this study, the bulk electrical resistivity of the mortar groups conditioned under the same aging environment was monitored as an evaluation of ASR and its mitigation.

Fig. 6a shows the evolutions of bulk electrical resistivity of the mortar cylinders immersed in 1 N NaOH solutions at room temperature for up to 150 days. It can be seen that the bulk electrical resistivity can be fitted well with the extended Freundlich equation with R^2 values of 0.959 (see Table 5). From Fig. 6a, the control group exhibits a relatively low bulk resistivity at a value of 23.7 Ω·m after 28 days, which became the lowest among the groups with a stable value of around 22 Ω·m from 60 days. This is in good agreement with the expansion and cracking results as discussed above that the severest ASR occurred in the control group and resulted in the highest permeability in the mortar matrix. The 0.74Li group showed a slightly higher value than the control group and increased from 23.9 Ω·m at 28 days to 28.8 Ω·m after 150 days. This provides an insight that lithium could improve the ASR resistance of concrete but with a limited efficiency, which is consistent with the ASR expansion (Fig. 3) and cracking observations (Figs. 4 and 5). It is interesting to find that, although the incorporation of 30 % fully saturated MK can suppress ASR expansion and cracking better than 0.74Li, a

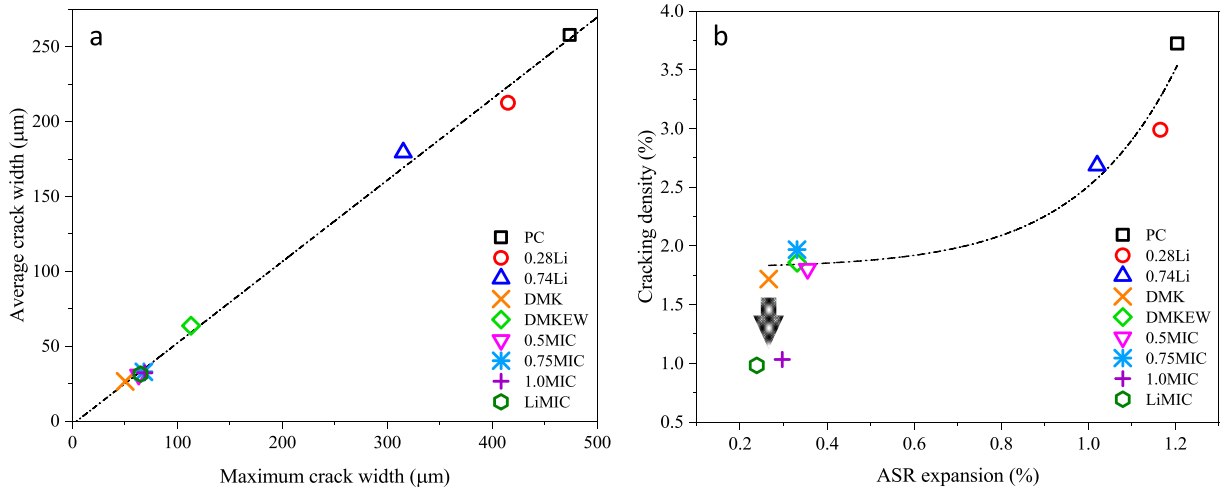

Fig. 5. (a) The relationship between the average and maximum crack widths and (b) correlation between cracking density and ASR expansion of the mortar bars.

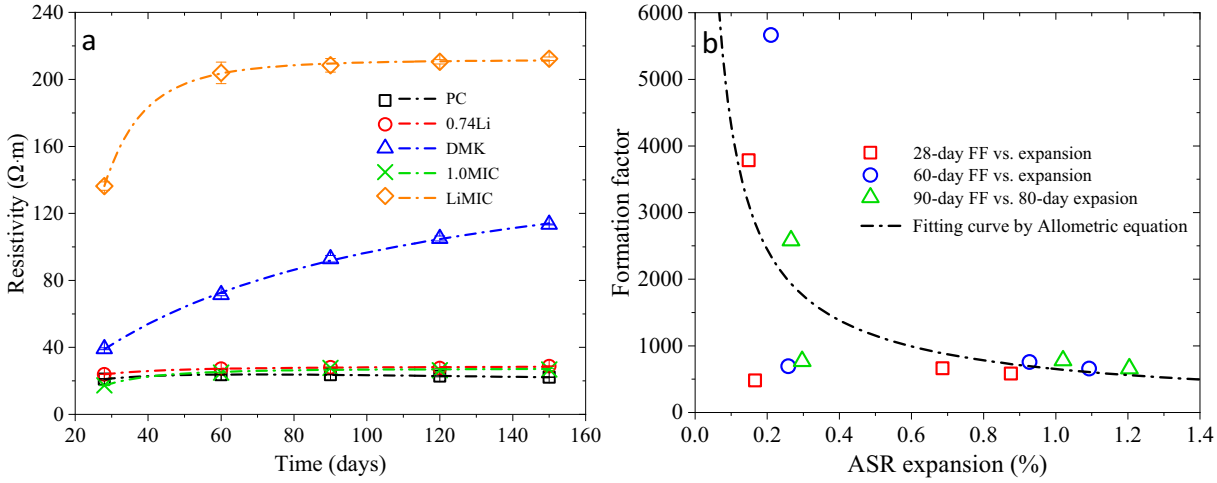

Fig. 6. (a) Developments of bulk electrical resistivity of mortars containing reactive aggregates with extended Freundlich fitting and (b) the relationship between the ASR expansion and formation factor.

Table 5
Freundlich fitting parameters of bulk electrical resistivity development.

$y = ax^{bx^c}$				
	a	b	c	R^2
PC	0.1998	3.073	−0.236	0.993
0.74Li	28.688	−30.306	−1.897	0.959
DMK	182.831	−11.025	−0.950	0.999
1.0MIC	27.25	−1165.03	−2.716	0.999
LiMIC	211.76	−12,118.9	−3.429	0.999

slightly lower bulk resistance at 28 days and 60 days and comparable values at later ages were observed in this test. The 1.0MIC group showed a 27.6 % lower electrical resistivity than the control group. Combining the observations from ASR expansion and cracking, this low bulk resistivity value is not because of low ASR mitigation but due to the high overall moisture content in the matrix of mortar supplied by the pre-saturated MK. However, it should be noted that the electrical resistivity of this group increased over time to a value of 26.4 Ω·m after 150 days, which is 15.7 % higher than the control group. The internal curing could gradually release water from the reservoirs and enhance cement hydration and pozzolanic reactivity and improve the microstructure in the later ages, but the electrical resistivity improvement is limited due to the additional water in the system. In contrast, with similar ASR suppression efficiency, the DMK group yielded an 86.3 % higher 28 days electrical resistivity than the control group, and it increased significantly over time.

It is again interesting to note that a remarkable synergistic effect between lithium and pre-saturated MK could be identified from the group of LiMIC, the bulk electrical resistivity of which is 136.3 Ω·m in 28 days, 6.5-fold of the control group, 5.7-fold of the 0.74Li group, and 7.9-fold of the 1.0MIC group. Moreover, this value exhibited a significant increase over time and enlarged the difference with other groups. After 90 and 150 days, the bulk resistivity of the LiMIC group increased to 208 Ω·m and 212.3 Ω·m, which are 8.8-fold and 9.6-fold of the control group, respectively. Compared with the low resistivity values from the 0.74Li group and the 1.0MIC group, the superior electrical resistivity of LiMIC revealed the coupled effect of these two additives in mitigating ASR and increasing the durability of concrete by probably improving the microstructure of the concrete, decreasing the deleterious ions diffusion, transportation, permeability within the concrete [59].

As shown in Fig. 6b, ASR-induced expansion decreased with the formation factor. After 150 days, LiMIC presents the highest FF of 5897.5, which is 9.6 times that of the control group at 150 days, indicating the lowest porosity and ion transport properties. The mortar with single incorporations of 0.74Li and 1.0MIC yielded FFs of 616.67 and 800.0, respectively, while the DMK group yielded a higher FF of 3150.3, which might be due to its low water content. These observations indicate that although ASR can be effectively mitigated by the pre-saturated MK and lithium, the addition of water for internal conditioning and lithium-ion can increase the conductivity of the matrix. This further reveals the superior performance of the co-existence of lithium and saturated MK in suppressing ASR and densifying the cement matrix.

3.4. Evolution of strength

Fig. 7 shows the development of compressive strength over time for the mortars containing lithium, dry and pre-saturated MK with different DOSs, and the one with coupled incorporation of lithium and MIC treated in saturated lime water for the first 28 days and the ones immersed in 1 N NaOH at 23 ± 2 °C for up to 90 days. The former was leveraged to understand the influence of the saturated MK on the strength development of cement composites without ASR, while the latter was used to uncover the role of saturated MK in mitigating strength loss in the presence of ASR. As shown in Fig. 7a, the 30 wt% partial replacement of cement with MK resulted in decreased compressive strength, which may be attributed to the dilution effect leading to a decreased fraction of C-S-H gel in the cement blends [65]. However, increased strength was detected from the groups with the addition of lithium. Because of the accelerated early-age cement hydration (the first 24 h), the 1-day compressive strength of 0.28Li is 12.7 % higher than the strength of PC. As reported by Millard and Kurtis [22], lithium nitrate can retard the cement hydration after 24 h, and therefore, the strength improvement after 7 days, 14 days, and 28 days were reduced, and a less effective strength improvement was observed when increasing the Li/[K + Na] ratio to 0.74. The DMK group yielded a compressive strength of 38.8 MPa on the first day, and this value was increased to 54.0 MPa at 28 days, which was 12.3% lower than the control group (PC). The same decreased compressive strength due to the high-volume incorporation of MK was also reported by the previous studies [66].

It can be seen in Fig. 7b that the strength of cement blends decreased with an increasing DOS of MK, which is not in conformity with the reduced CH content and increased amounts of C-S-H and strätlingite. Nevertheless, from 1 day to 28 days of hydration, the compressive strength of 0.5, 0.75, and 1.0MIC groups increased by 83.9 %, 75.8, and 159.6 %, respectively, while the DMK group only increased by 39.5 %. Moreover, the DMKEW group showed a 0.6 % to 19.6 % lower compressive strength than the 1.0MIC group at all the testing ages.

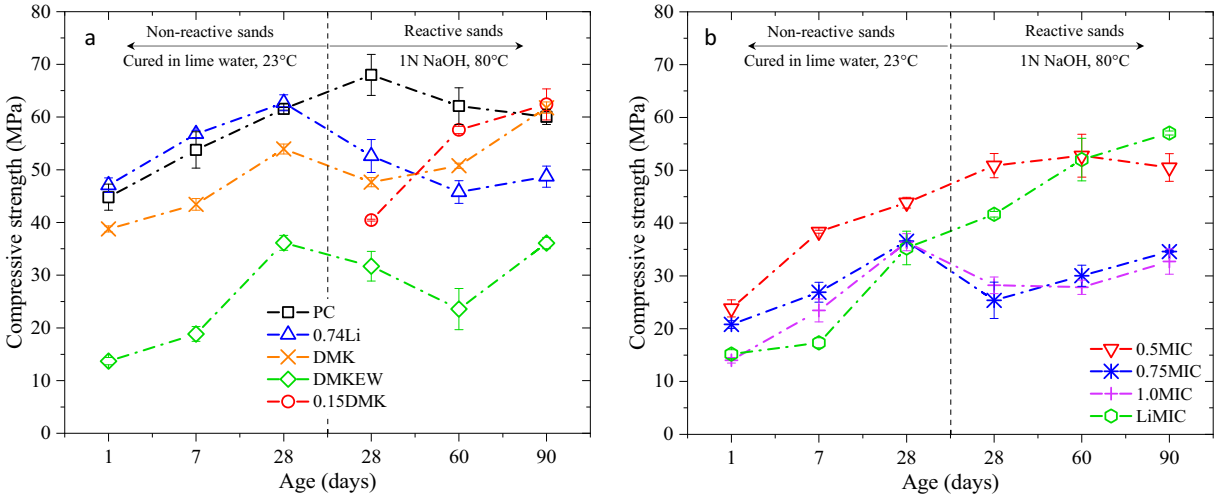

Fig. 7. Compressive strength development of mortars with non-reactive sand and cured in saturated lime water and mortars with reactive sand and cured in 1 N NaOH solution at 23 ± 2 °C: (a) control group and the groups with lithium or dry MK and (b) MIC and LiMIC groups.

Although the compressive strength of mortars was decreased due to the increased water content introduced by saturated MK, a higher strength gain rate was obtained. The coupling effect of lithium nitrate and pre-saturated MK is also exhibited in Fig. 7b. It shows that the addition of lithium nitrate yielded an 8.4 % higher 1-day strength than the 1.0MIC group, probably resulting from the acceleration effect of lithium during the first-day cement hydration. However, at 28 days, the strength of LiMIC was 3.0 % lower than that of 1.0MIC, which might be due to the retarding effect of lithium in cement hydration.

From the mortars cast with reactive aggregates immersed in 1 N NaOH solutions, it can be seen that the compressive strength of the control group was decreased by 11.7 % from 28 days to 90 days, due to ASR deterioration. The same negative effect has also been observed in previous investigations [11,67]. A decreased compressive strength was also observed from the 0.74Li group. Although lithium can help mitigate ASR to a certain extent, it retards cement hydration after 1 day and can increase shrinkage of the cement paste, which is opposite to the volume expansion induced by ASR, negatively impacting the strength development in the presence of accelerated alkaline-aging treatment. This again indicates the necessity of investigating the long-term efficiency of lithium in ASR suppression, especially in concrete containing highly reactive aggregate that serves under extreme conditions. Contrary to the decreased compressive strength in the control and 0.74Li groups, a continuously increased strength was observed from the DMK group. At 28 days, the incorporation of 30 % dry MK decreased the strength by 29.9 %, followed by a 90 days strength exceeding the control group. It is worth noting that the inclusion of MK as cement substitution can improve the compressive strength of mortar and concrete only at an optimum dosage between 10 %–20 % [33]. With a too low or too high cement replacement level, the MK will either exhibit the benefit of pozzolanic reaction less than enough to improve the strength and durability properties of concrete or yield a low degree of reaction, which in turn negatively compromises concrete performance. Keep this in mind, a group with 15 % dry MK (0.15DMK) was tested here, which yielded a strength lower strength at 28 days and higher strength at later ages than the DMK group. These observations again confirmed the benefits of MK in mitigating ASR at appropriate dosages, especially at later ages. It should be noted that the alkaline treatment employed in this study might also enhance the role of MK in the cement system through alkaline activation reactions, as both the dissolution of MK and cement hydration can be enhanced in the presence of alkalis [68].

The 0.5MIC group exhibited a strength of 50.9 MPa after 28 days, which is 6.8 % higher than the DMK group but 25.2 % lower than the control group. After 60 days and 90 days' conditioning, this group yielded strength higher than the 0.74Li group but lower than the control and DMK groups. The phenomenon can also be observed from the other two groups containing pre-wetted MK, i.e., the 0.75MIC and 1.0MIC groups, that the absolute compressive strength of the groups with pre-saturated MK is lower than the control group, but increased strength over time can be obtained from these groups. However, compared with their 28-day strength, these two groups yielded a strength gain of 36.4 % and 15.9 % after 90 days of alkali treatment, respectively, indicating the low contribution of highly saturated MK to the early-age strength, but the water was gradually released at a later age as a function of internal curing can compensate this negative impact and offset the ASR-induced strength loss.

Moreover, the compressive strength of the DMKEW group is 31.7 MPa, 23.6 MPa, and 36.1 MPa after 28 days, 60 days, and 90 days' treatment, respectively, which are comparable or even slightly higher than both the groups containing 0.75MIC and 1.0MIC. This might be due to the excessive amount of internal curing water in the groups with highly saturated MK (0.75MIC and 1.0MIC) at the high cement substitution level (30 %). As reported by Bentz and Weiss [69], it is necessary to appropriately design the internal curing process, including the amount of internal curing water, the distance of the migration of the internal curing water into the surrounding cement paste, and the distribution of the internal curing agents within the three-dimensional structure of the mortar or concrete, for reaching the optimum effect on the performance and durability of concrete. Based on the results, a lower degree of saturation and a lower MK dosage that can yield a more reasonable amount of internal conditioning water in the cement system is recommended for better compressive strength gain of the concrete. However, the negative impact of saturated MK on strength gain was offset by the supplementary addition of lithium and its synergistic effect with MK. As shown in Fig. 7b, the LiMIC group yielded a 28-day strength of 41.7 MPa, which is lower than the control group and 0.74Li, but higher than the 1.0MIC group. After 90 days' immersion in 1 N NaOH solution, the strength was increased to 57.1 MPa, which is 17.15 % and 74.41 % higher than 0.74Li and 1.0MIC, and only 5.0 % lower than the control group. In addition to the excessive water supplied by the high dosage of saturated MK, it should also be noted that, in this study, the mortar specimens were invariably treated in the alkaline solution that can continuously provide external water for curing. Treated in this conditioning, the unique benefit of internal curing in the groups containing pre-saturated MK cannot be fully achieved, and it might adversely impact the evolution of the mechanical strength of the mortars. Under such a condition, the significant strength increase was still observed from the ternary mortar containing both lithium and saturated

MK, which is compelling evidence of the unique coupling effect between the two additives in mitigating ASR.

3.5. Microstructural analysis

In previous studies, the formations of two ASR gels were discussed based on their textures: the first one is crystalline, which is predominantly appears inside the aggregate particles, and the other one is amorphous, primarily resides along the particle edges, paste cracks, and inside voids [70]. In this study, the microstructure of the selected mortar bar specimens after 80 days of treatment was analyzed using SEM equipped with EDS. The formation of ASR gel inside a crack running through an aggregate and the cement matrix in the control group was confirmed in Fig. 8. As shown in Fig. 8a, an apparent crack formed inside the aggregate filled with ASR gel was observed. In the magnified microscopy figure (Fig. 8b), the ASR gel's amorphous morphology, microcracks, and a fragment of the aggregate at the edge of the cracks were observed, indicating the destructivity of the ASR gel.

EDS analysis was performed at two zones for the specimen, as shown in Fig. 8a and b, to determine elemental compositions of different phases. The detections were conducted for the cement paste and ASR gel inside the crack. As shown in Fig. 8c, Zone 1 shows a Ca/Si ratio of 1.12, which indicates the detected area is the cement matrix, especially the C-S-H gel, agreeing well with the C-S-H composition obtained from previous studies [71,72]. In contrast to the cement paste, a Ca/Si ratio of 0.46, which is nearly equal to the values of ASR products presented by [70], was detected in zone 2, indicating that the phase is an ASR gel. The presence of alkalis, such as potassium and sodium, typically contained in ASR gels was also detected. It was also reported that low-calcium ASR gel could be converted from C-S-H produced in the presence of dissolved silica near the reactive aggregate grain via local depletion of portlandite [73]. After the exhaustion of portlandite, the concentration of silicon of the ASR gel increased rapidly due to the continuous dissolution of silica from the reactive aggregates [74], thereby yielding a low Ca/Si ratio. Moreover, a minor amount of aluminum yielding an Al/Si ratio of 0.08, which is lower than that of the cement paste (0.16), was also detected from the ASR gel. This minor aluminum detected from the ASR gel, which is comparable to a previous study by Bektas and Wang [11], might be due to the involvement of aluminum in the process of ASR in the studied mortar system or its migration from the surrounding cement paste into the ASR gel.

Since there is no ASR gel and cracks can be detected from the cross-sections of other groups, only the microstructure of the DMK and 1.0MIC groups are presented here. Compared with the control group, a denser structure can be observed from the mortar containing 30 % dry MK. Even after 80 days of accelerated aging treatment in 1 N NaOH solution at 80 °C, no microcracks can be detected from the cross-section. The EDS analysis shows Ca/Si ratios of 0.94 and 1.10 for the phases formed in the rectangles of Fig. 9a, indicating the formation of C-S-H in the cement paste. Due to the incorporation of MK, the content of aluminum is higher than that detected in the control group. As discussed in the previous publications [75,76], MK can consume CH and form additional C-S-H gel and the modified C-S-H gel containing aluminum (i.e., C-A-S-H), leaving less calcium for the formation of ASR gels, which is another ASR mitigation mechanism.

Fig. 10a and b show the microstructure of the mortar containing 1.0MIC. It can be observed that the cement binder has a dense structure, but microcracks were found in the aggregate area. EDS analysis was conducted at four distinct locations to determine the composition of the phases inside the crack (i.e., zone 2, zone 3, and zone 4 in Fig. 10) and the cement paste (i.e., zone 1 in Fig. 10). As shown in Fig. 10c, a Ca/Si ratio of 1.04 was detected in zone 1 with a high concentration of

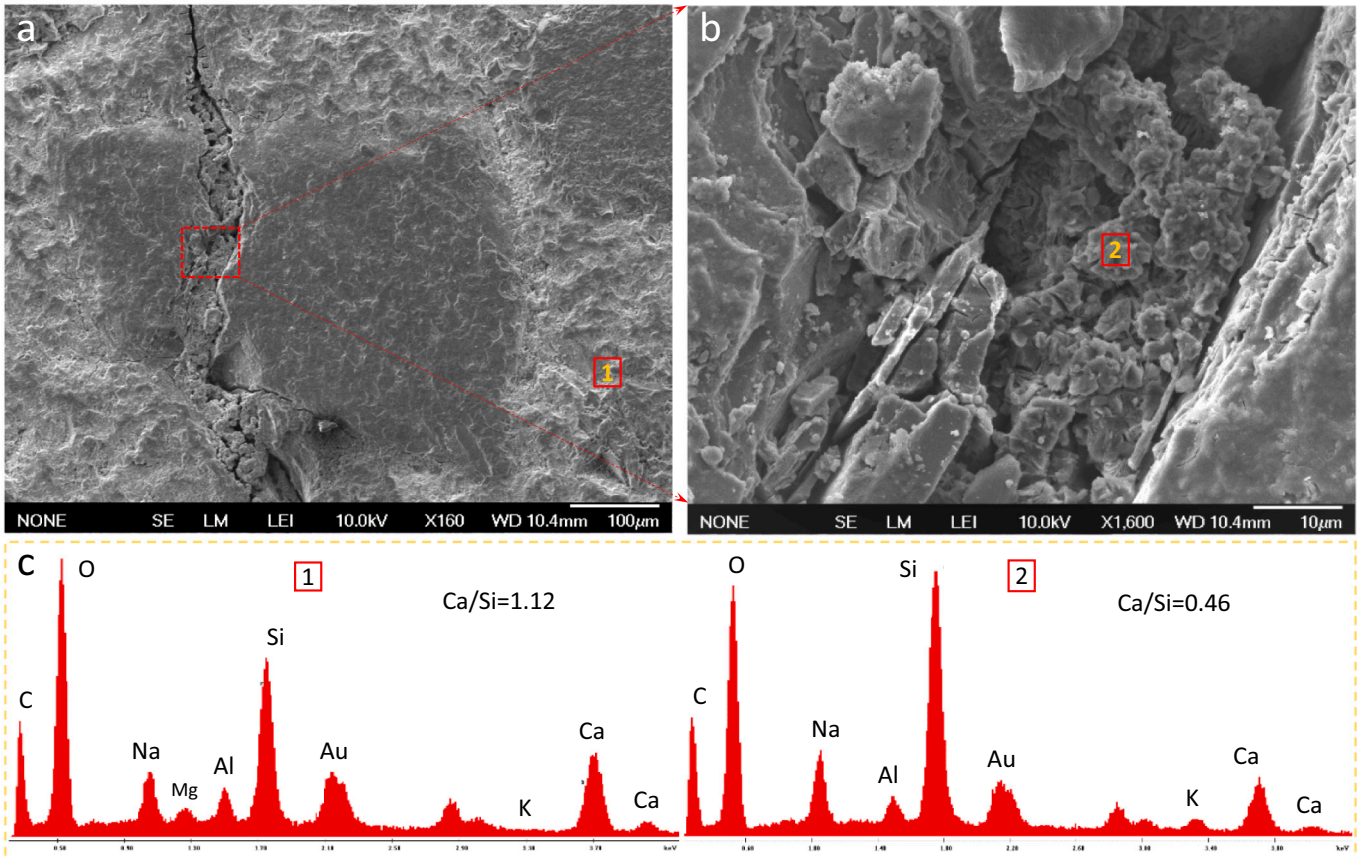

Fig. 8. Microstructure of the control group after 80 days of immersion in 1 N NaOH at 80 °C: (a) a microcrack inside aggregate filled with ASR gel, (b) magnified area of ASR gel, and (c) EDS spectra of the ASR gel (zone 1) and the cement matrix (zone 2).

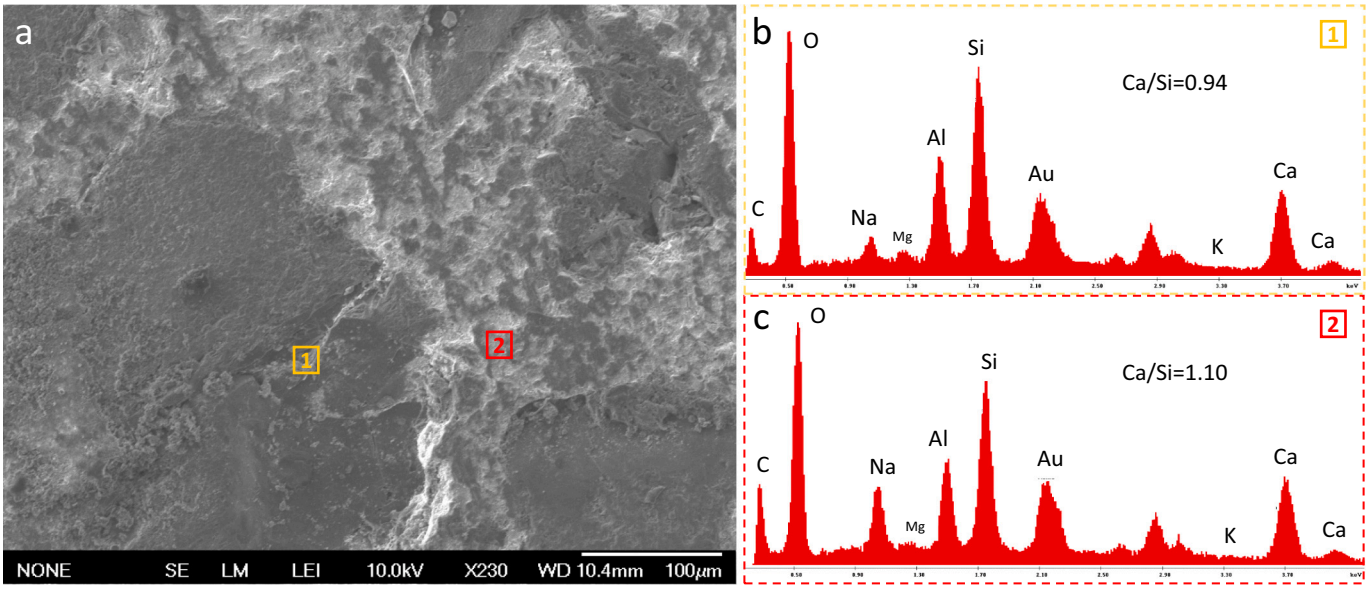

Fig. 9. (a) Micromorphology and (b) EDS analysis of the DMK group after 80 days of aging treatment.

aluminum, indicating the formations of C-S-H or C-A-S-H phases in the cement matrix, which are similar to the findings from the DMK group. The low Ca/Si ratios of 0.05, 0.18, and 0.02 without potassium and sodium at zone 2, zone 3, and zone 4 indicate that there is no ASR gel formed in the microcracks of aggregates. The cracks might be the intrinsic grain boundary and defects of the aggregates rather than a result of ASR.

3.6. Discussion of mitigation mechanisms

To elucidate the mechanisms of ASR mitigation triggered by MIC, the two most critical prerequisites of ASR deterioration, (i) silica dissolution from the reactive aggregates that dominates the formation of ASR gels and (ii) the property evolutions of ASR gels that govern the destructive nature of ASR, were investigated. The silica dissolution under the attack of OH^- ions is widely considered the first and slowest step of the ASR process and thereby dominates the ASR rate in concrete [3]. By suppressing the silica dissolution rate, the concrete's ASR-induced damage could be effectively mitigated or even eliminated. However, due to the extremely high reactivity of the sands used in this study, the dissolution of silica and the formation of ASR are unavoidable. Therefore, the suppression of silica dissolution rate and conversion of ASR properties were studied. In concrete containing reactive aggregates, ASR gel is typically featured with high porousness, high surface area, and high stiffness attributed to the calcium incorporation, making it a hygroscopic and expansive phase capable of absorbing moisture, swelling, and thereby creating destructive internal stresses in concrete. With the purpose of obtaining insights on the diminished destructivity of ASR gel in the presence of MIC, the evolutions of chemical phases, static and dynamic moisture absorption kinetics, and swelling behavior of ASR gels were studied.

3.6.1. The roles of lithium and aluminum in mitigating silica dissolution behavior

Figs. 11 and 12 show the development of silicon concentrations dissolved from the reactive sands with particle sizes smaller than 150 μm (sand-1, Figs. 11a and 12a) and in the range of 300 μm–600 μm (sand-2, Figs. 11b and 12b), respectively, in the simulated pore solutions with different amounts of lithium and aluminum up to 28 days. The correlation between the dissolved silicon concentrations and the dissolving time up to 336 h can be impeccably fitted with the modified Weibull cumulative distribution function (CDF) with R^2 values over 0.968 (see Table. 6). However, a jump of silicon concentration occurs in all cases at 672 h, which results in a significant deviation from the fitting curves. This might be induced by the damage of the reactive aggregates due to the long-term alkali attack, which resulted in new surfaces with additional amorphous silica exposure.

In the control pore solution without the addition of lithium or aluminum, rapid increases in silicon concentration during the first 24 h were obtained from both sand-1 and sand-2, which reached equilibrium after 168 h. Compared with sand-2, 42.9 % more silica was dissolved from sand-1 during the first 24 h, which might be due to the larger contact surface of the sand with a smaller particle size that facilitates the dissolution rate of the amorphous silica in pore solution. It is worth noting that the silicon concentration increased slowly from 168 h to 336 h but turned sharply at 672 h in all the groups. The slowed-down silicon dissolution might be caused by the precipitation of Ca—Si phases on the sand surfaces [77]. On the contrary, the sharply increased silicon concentration in the later ages might be induced by the corroded aggregate grains, which triggers additional exposure of new reactive silica sites to the pore solution.

In the pore solution containing lithium, an accelerated silica dissolution during the first 24 h was observed (see Fig. 11a and b). The concentration of silicon in the pore solutions was found to increase with the dosage of lithium during the first 6 h, which is more significant for sand-1. As a result, in the solutions of 0.5Li, 0.75Li, and 1.0Li, 2.8 %, 8.3 %, and 25 % more dissolved silicon were detected from sand-1 after 6 h than that in the control pore solution. Interestingly, the dissolution rate of silica was slowed down in the presence of lithium after 24 h. This might be due to the formation of a Li—Si network formed by the reaction between the silica species and the lithium ions in the solution, which serves as a barrier layer against dissolving silicon from the reactive chert of the aggregate [78]. This explains the accelerated silica dissolution during the first day, as the silica dissolution is needed to trigger the formation of the Li—Si layer. This is particularly the case of sand-1 (see Fig. 11a), where the silicon concentration exhibited a negative correlation with the lithium dosage. After 336 h, compared with the one immersed in the control pore solution, 15.7 %, 14.1 %, and 4.3 % less silicon was dissolved from sand-1 in the presence of 0.5, 0.75, and 1.0 Li/[K + Na] ratios, respectively. This finding indicates that the optimum Li/[K + Na] ratio in suppressing dissolutions of amorphous silica from the reactive aggregate in the cement matrix is 0.5 to 0.75, and a higher

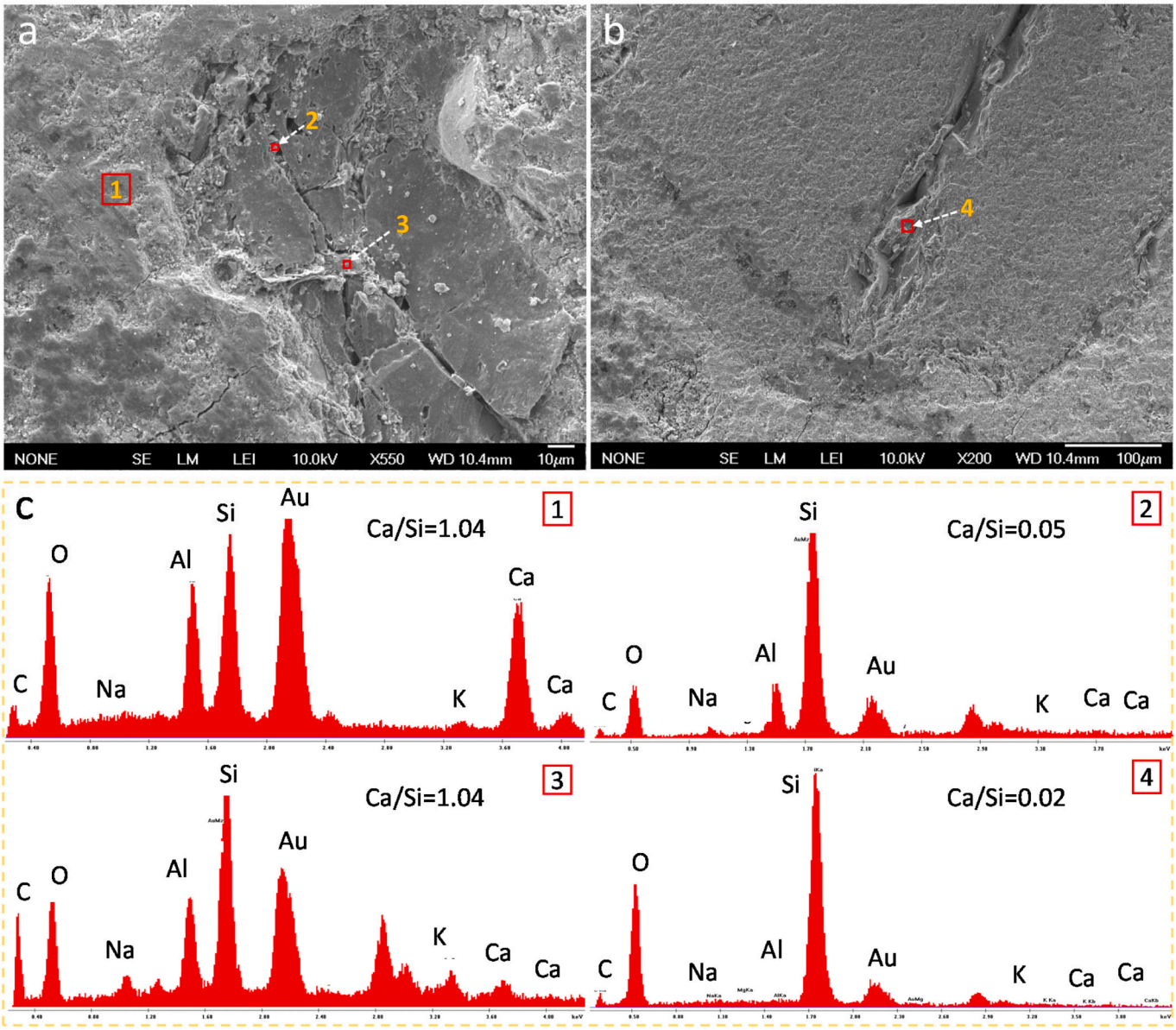

Fig. 10. (a, b) Microcracks in aggregates and (c) EDS analysis of the phases in the 1.0MIC group after 80 days of accelerated aging treatment.

lithium content does not result in better results, which agrees with [79]. Effective mitigation of ASR expansion was also obtained from higher Li/[K + Na] ratios of 0.72 to 0.93, as about 40 % of lithium can be absorbed by the cement hydration products [80]. However, the efficiency of lithium in mitigating silica dissolution showed a strong dependence on the aggregate size. Different from the observations in sand-1, the silica dissolution of the coarse sand can be decreased only when the Li/[K + Na] ratio reaches 1.0. As shown in Fig. 11b, at lower lithium dosages, more silica was dissolved from sand-2. After 28 days of dissolution, although with a significant jump, for sand-1, the silicon concentrations of the pore solutions containing lithium are still lower than that of the control pore solution, which again decreases with the decreasing lithium dosage. However, sand-2 yielded a similar degree of dissolution in the control and 0.75Li pore solutions. When the Li/[K + Na] ratio was increased to 1.0, 39.5 % less silicon was dissolved from this coarse sand.

An opposite yet interesting phenomenon was observed from the pore solutions containing aluminum (Fig. 12). Different from lithium, a significant decrease in silica dissolution in the presence of aluminum was detected during the first 7 days, especially the first 24 h. A second difference between aluminum and lithium is that more significant mitigation of silica dissolution was obtained from the coarser sand-2. As a result, in the pore solutions containing 2.73 mmol/L, 6.4 mmol/L, and 10.0 mmol/L aluminum, the 24-h silica dissolution of sand-2 was decreased by 35.9 %, 33.0 %, and 29.7 %, respectively, while 25.0 %, 35 %, and 20.0 % less silica was dissolved from sand-1. Although silica dissolution from 24 h to 168 h is still slower in the pore solutions containing aluminum, the dissolution rate increases. This is especially the case for sand-2, in which the silicon concentration difference between the control and 2.73Al pore solution decreased from 35.9 % at 24 h to 6.8 % at 168 h. This again indicates that aluminum can play an effective role in suppressing silica dissolution during the initial stages. After 7 days, a more efficient silica dissolution mitigation of aluminum was obtained from the finer sand-1, in which the silicon concentration in the pore solution with 2.73 mmol/L aluminum reaches equilibrium with no further increase over time. Interestingly, the addition of more aluminum resulted in higher silica dissolution.

From 14 days, the silica dissolution of sand-1 in the presence of aluminum is still lower than that in the control pore solution, while silicon concentrations in the presence of aluminum exceeding that in the control pore solution were observed from sand-2. According to [49,50],

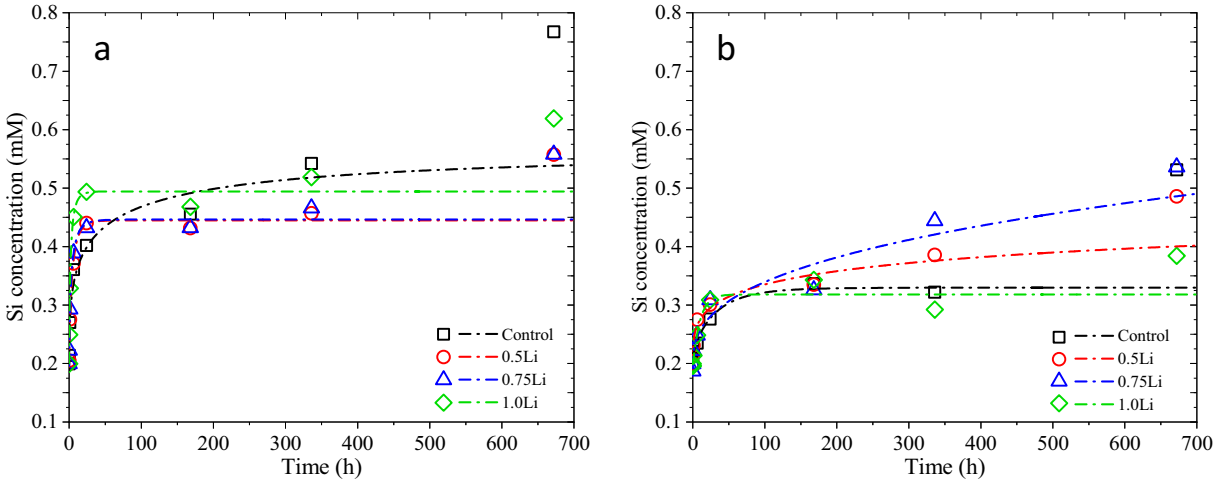

Fig. 11. Silica dissolution from reactive (a) sand-1 and (b) sand-2 in pore solutions with varying lithium concentrations and the Weibull CDF fitting curves for the first 14-day data.

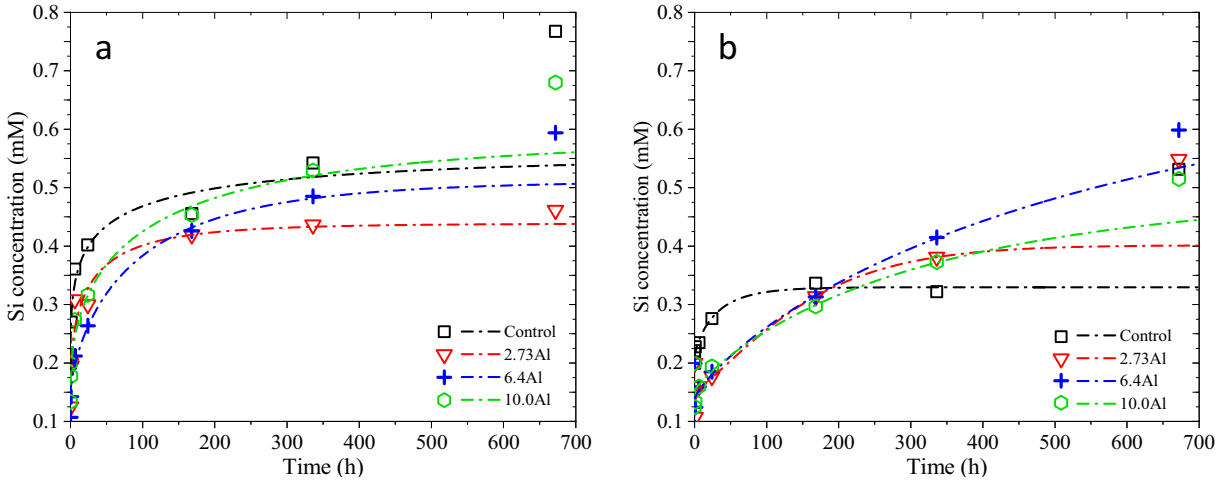

Fig. 12. Silica dissolution from reactive (a) sand-1 and (b) sand-2 in pore solutions with varying aluminum concentrations and the Weibull CDF fitting curves for the first 14-day data.

Table 6
Weibull fitting parameters of the first 14-day silica dissolution from the reactive sands.

	Sand-1					Sand-2				
	y_0	A_1	a	b	R^2	y_0	A_1	a	b	R^2
Control	0.189	0.374	41.174	0.361	0.968	0.212	0.118	31.106	0.842	0.973
0.5Li	0.194	0.251	4.296	0.737	0.992	0.196	0.312	543.88	0.309	0.977
0.75Li	0.196	2.500	3.334	0.642	0.990	0.193	1242.85	6.3×10^{12}	0.364	0.923
1.0Li	0.200	0.294	2.274	0.662	0.987	0.198	0.120	10.305	1.036	0.934
2.73Al	0.163	0.276	28.639	0.550	0.908	0.154	0.248	162.76	1.263	0.926
6.4Al	0.149	0.363	94.640	0.721	0.956	0.139	0.588	591.63	0.822	0.915
10.0Al	0.163	0.426	108.96	0.538	0.964	0.153	0.339	321.73	0.877	0.929

aluminum in the pore solution can retard the initial silica dissolution rate, but the final amount of dissolution cannot be decreased. This can be explained by the findings from [47] that no significant difference in silicon concentration was observed with the aluminum concentration between 3.9 mmol/L and 35 mmol/L unless a continuous aluminum reserve was provided, as the aluminum in pore solution can be depleted quickly. In this study, the three investigated aluminum concentrations are in the discussed ranges with no additional supply, the fast exhaustion of which might be the reason for the rising silicon concentrations. This also indicates that the efficiency of MIC in suppressing silica dissolution in the matrix of cement might be underestimated by employing aluminum concentrations between 2.73 mmol/L and 10.0 mmol/L as the continuous release of aluminum from MK and the aluminum-rich hydration products might sustain its effective role.

As discussed above, lithium and aluminum play different roles in mitigating silica dissolution, where lithium can increase the initial silicon concentration but shows a high efficiency at later ages, while a reversed phenomenon was observed from aluminum. These findings

explain the optimum ASR mitigation from the LiMIC group, where lithium and aluminum synergize to decrease the silica dissolution at both early and later ages. Furthermore, the silica dissolution mitigation roles of both lithium and aluminum vary with aggregate sizes with a decreased efficiency over time, which indicates that the mitigated ASR expansion and cracking might also be attributed to changes in ASR products.

3.6.2. Influences of lithium and aluminum on phase evolution of ASR gels

3.6.2.1. Thermogravimetric analysis. Fig. 13 shows the TGA and differential thermogravimetric (DTG) curves of the control synthetic ASR gel with Ca/Si, K/Si, and Na/Si ratios of 0.5, 0.2, and 0.8, respectively, and three ASR gels modified with lithium, aluminum, and their combination at Li/[K + Na] and Al/Si ratios of 0.3, after 28 days of reaction. No weight loss from TGA and DTG peak corresponding to the decomposition of CH was detected in the control group indicating the complete consumption of this raw material after 28 days, while a small peak for CH can be found from the groups containing either lithium or aluminum, which revealed the mitigated ASR. Two main weight losses could be identified from the control sample: the first weight loss between 30 °C and 200 °C corresponds to the evaporation of free and loosely bound water, while the second weight loss between 230 °C and 360 °C indicates the loss of chemically bound water from ASR-P1 ($K_{0.52}Ca_{1.16}Si_4O_8(OH)_{2.84}\cdot 1.5H_2O$), a nano-crystalline ASR product with a silica structure dominated by Q^3 species [81]. From the sample containing lithium, an increased first weight loss was observed, but the second one disappeared. This indicates the positive role of lithium in suppressing the formation of ASR gels. Two DTG new peaks, one between 600 °C and 750 °C and one between 760 °C and 860 °C emerged suggesting the decomposition of sodium nitrate [82] and lithium orthosilicate (Li_4SiO_4) [83], respectively. Although lithium orthosilicate was not detected by XRD at 28 days, it appeared after 180 days of reaction, see Fig. 15 below. From the sample containing aluminum, the first weight drop due to the loss of free and loosely bound water increased and shifted to a lower temperature range of 30 °C to170 °C. A new weight loss at around 235 °C appeared, which might be due to the decomposition of gibbsite (AH_3) in the presence of aluminum [84], which was also detected from the XRD below. However, the peak at 280 °C corresponding to the ASR products was still observed, indicating the addition of aluminum may not be able to completely convert the final formation of ASR gels, which is in agreement with [85]. The coupled addition of lithium and aluminate with the same dosage used above (Li/[K + Na] of 0.3, Al/Si of 0.3), the first peak due to the evaporation of free and loosely bound water shifted back to the temperature of around 125 °C, but with a lower intensity than both the lithium and aluminum groups. Moreover, the DTG peaks due to the decompositions of gibbsite and ASR products (ASR-P1) disappeared, indicating 1) the enhanced absorption of aluminum in C-S-H phases to form aluminum-rich phases in the presence of lithium; and 2) a synergistic effect between lithium and aluminum in mitigating the formation of ASR gels. The formations of sodium nitrate and lithium orthosilicate were still detected, but they both shifted to higher temperatures. It was reported that the thermal stability of sodium nitrate could be improved with the presence of colloidal silica [82], as the sodium nitrate could be embedded in the silica porous network structure. This indicates that more colloidal silica was remained in the matrix when both lithium and aluminum were incorporated.

3.6.2.2. X-ray diffraction analysis. The XRD patterns of the synthetic ASR gels with and without lithium and aluminum after 28 days of reaction are shown in Fig. 14a. The broad peaks at ~29.2° and ~31.7° 2θ are assigned to the semi-crystalline tobermorite-type phase, which is considered a typical ASR gel [74,86]. The fedorite ($KNa_4Ca_4Si_{16}O_{36}(OH)_4\cdot 6H_2O$) phase at ~50° 2θ is also an indication of a semi-crystalline ASR product [87]. It can be seen that the lower intensity of ASR products was observed from the lithium group and aluminate group indicating the effective suppression of ASR gels' formation. A synergistic effect between lithium and aluminum in mitigating the formation of ASR gels was identified from the lowest intensity of the ASR gels-related peaks among all the groups. Compared with the control group, higher CH peaks at ~18.0°, ~34°, ~47°, ~50.7°, ~54.4°, and ~59° 2θ were detected from the samples with the addition of either lithium or aluminate, while lithium shows higher efficiency than aluminum. In line with the observations in CH, suppressed consumption of amorphous silica (peaks at 37.6°, 38.8°, and 41° 2θ correspond to silica [88]) was also observed in the groups containing lithium and aluminum. It is noteworthy that the reactions among calcium, silica, and alkalis are the major prerequisite of ASR deterioration, and the consumption of CH and amorphous silica are directly associated with the precipitation of the ASR products [86]. Therefore, in addition to the step-down silica dissolution rate, the remaining two reactants provide a second strong indication that both lithium and aluminum can mitigate ASR. From the intensity of relevant peaks, lithium might play a more significant role. In the presence of coupled lithium and aluminum, the lowest ASR products (tobermorite and fedorite) peaks and the highest intensity of silica and CH peaks were obtained, suggesting the most noticeable ASR mitigation efficiency. New peaks at 35.6° and 39.5° 2θ associated with hydrogarnet and ~50.09° 2θ for gibbsite (AH_3) were observed [89], indicating the conversion of ASR gels into more stable aluminum-containing phases

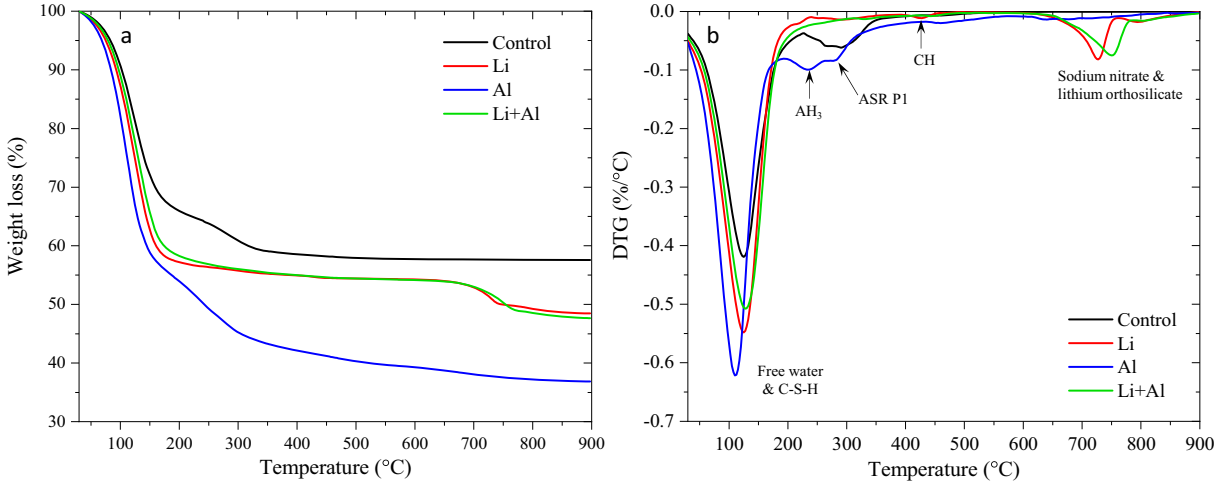

Fig. 13. TGA/DTG curves of ASR products after 28 days of reaction.

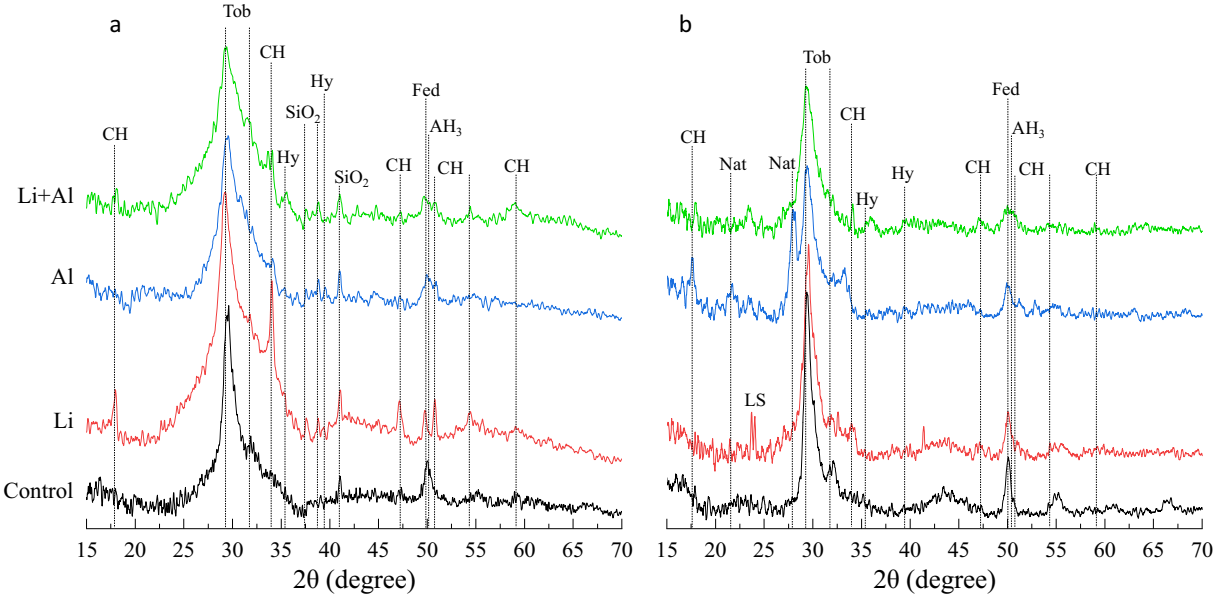

Fig. 14. XRD patterns of ASR gels after (a) 28 days and (b) 180 days of reaction. CH: calcium hydroxide, Tob: tobermorite, Hy: hydrogarnet, Fed: fedorite, Nat: natrolite, AH_3: gibbsite, LS: lithium (ortho)silicate.

[90].

After 180 days of reaction, as shown in Fig. 14b, the peaks of CH of the control group disappeared, while the peaks of tobermorite and fedorite became sharp with increased intensity indicating the high extent of ASR and the formation of more well crystalline ASR products. In the presence of lithium, semi-crystalline tobermorite and fedorite with lower peak intensity than that at 28 days were detected. A new peak at ~23.99° 2θ due to the formation of lithium orthosilicate was also detected. Comparing the observations at 28 days, the groups containing aluminum (Al and Li + Al) showed new peaks at 21.63° and 27.97° 2θ caused by the formation of aluminum-bearing natrolite (sodium tecto-alumosilicate hydrate, $Na_2Al_2Si_3O_{10}{\cdot}2H_2O$) after 180 days. Due to the formations of these new phases, no silica peaks can be detected after 180 days. The evolutions of the CH, tobermorite, and fedorite peaks from 28 days and 180 days reveal the higher efficiency of aluminum than lithium in mitigating the formation of ASR gels, while the combination of lithium and aluminum shows the optimum performance, which agrees well with the suppressions in ASR expansion and cracking.

3.6.2.3. Attenuated total reflection-Fourier transform infrared spectroscopy. Fig. 15a and b display the ATR-FTIR spectra of the ASR products after 28 days and 180 days, respectively. To avoid the potential influence of drying on the molecular structure and chemical bonds of ASR gels, the samples were not dried before testing thus the peak at ~1640 cm^{-1} assigned to υ_2 bound water retained in the mixtures [91] was observed. The lower peak intensity of the water molecules from the samples containing lithium and aluminum might be due to the higher water consumption in these systems to form more hydration products over the pure ASR gels. The peaks at ~1252 cm^{-1} and 1158 cm^{-1} were assigned to Si-O-Si asymmetric vibrations [92], peaks at ~840 cm^{-1} and 832 cm^{-1} correspond to the stretching vibrations of the Si—O bonds [93], while 1360 cm^{-1}, 652 cm^{-1}, 530 cm^{-1}, 478 cm^{-1} and 433 cm^{-1} to O—Si—O bending vibrations [94]. Moreover, the peaks at ~968 cm^{-1} and 963 cm^{-1} were reported as Si—O stretching vibrations from shlykovite [95]. These Si—O—Si vibrations suggest the formation of more non-expansive Q^2 C-S-H phases in the presence of lithium and aluminum, while lithium exhibited a more pronounced efficiency. Interestingly, the highest peaks of non-expansive C-S-H phases were

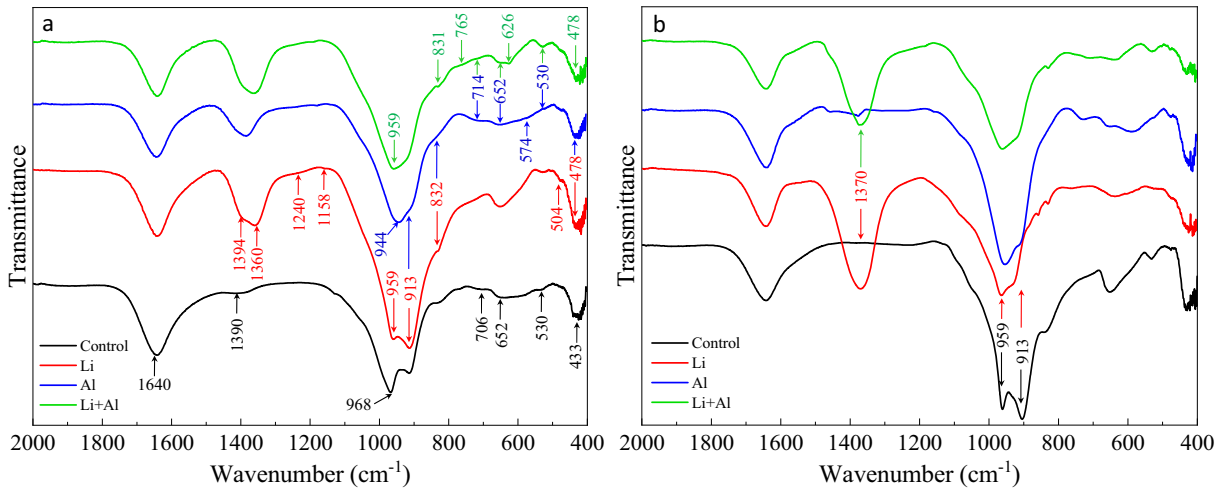

Fig. 15. ATR-FTIR spectra of ASR products after (a) 28 days and (b) 180 days of reaction.

obtained from the group with coupled lithium and aluminum, indicating the synergistic effect between these two additives in converting expansive ASR gels into non-expansive phases. In the presence of aluminum, the peak of Si—O stretching at around ~960 cm^{-1} shifts to a lower frequency of 944 cm^{-1}, revealing the substitution of silicon with aluminum in the precipitated products [96]. The peak at ~765 cm^{-1} from the group containing both lithium and aluminum is also assigned to the Si—O—Al bond from C-A-S-H [97]. The ASR (Q^3) phases associated with the peaks at ~913 cm^{-1}, ~652 cm^{-1}, ~626 cm^{-1}, and 504 cm^{-1} [95], the primary reason for hygroscopic swelling [98], were detected from the control group. While some of these ASR gel peaks were still detectable in the lithium and aluminum groups, significant decreases in the peak intensities were observed, indicating the effective ASR mitigation by using lithium or aluminum. After 180 days, the peak intensity of the ASR (Q^3) phase increased dramatically in the control group (Fig. 15b) indicating the continuous formation of ASR gels. In the presence of lithium, increased C-S-H peak at ~970 cm^{-1} and decreased ASR peak at ~913 cm^{-1} over time were observed, which might be due to the conversion of ASR gel to C-S-H gel. With the continuous reaction with aluminum, decreased or even eliminated intensity of the peak between 1360 cm^{-1} and 1395 cm^{-1} was observed from the control and aluminum groups after 180 days, while this peak presented in the lithium-modified ASR gel might be due to the Si—O—Si vibrations in Q^2 C-S-H phases or the N—O stretching vibration from nitrate. Both the peaks at ~913 cm^{-1} and 504 cm^{-1} disappeared, and only two minor peaks at ~652 cm^{-1} and ~626 cm^{-1} remained after 180 days in the group with the co-existence of lithium and aluminum, revealing the synergistic effect of lithium and aluminum in mitigating the formation of expansive ASR products, which is consistent with the TGA and XRD results and the ASR mitigation above.

3.6.3. *The roles of lithium and aluminum in altering hygroscopicity of ASR gels*

3.6.3.1. Static moisture absorption. The O—H stretching between 3690 cm^{-1} and 2400 cm^{-1} and bending at ~1640 cm^{-1} assigned to the water molecules under ATR-FTIR were leveraged to assess the static moisture absorption behavior of the ASR gels under a specific RH by monitoring the evolutions of peak intensity. Fig. 16 shows the ATR-FTIR spectra of the ASR gels after exposing 97 % RH in a wavenumber range of 4000 cm^{-1}–1500 cm^{-1}, from where a noticeable increase in the peak intensity caused by the absorbed water over time is observed from all the ASR gels. The control ASR gel without lithium or aluminum exhibited a significant water absorption after only 10 min. The intensity of the two peaks at 3690 cm^{-1}–2400 cm^{-1} and ~1640 cm^{-1} increased by 10.8 % and 5.2 %, respectively. This quick moisture absorption indicates robust hygroscopicity, which reaches equilibrium after about 7 h. By introducing lithium at a Li/[K + Na] ratio of 0.3, no significant water absorption was detected during the first 1 h, indicating the effective role of lithium in altering moisture absorption kinetics of the ASR gel. Considerable increases in the two peaks (3690 cm^{-1}–2400 cm^{-1} and ~1640 cm^{-1}) were observed from 4 h, which are still 30.1 % and 11.4 % lower than that of the control group at the same period, respectively. As a result, in the presence of lithium, the time to reach moisture equilibrium in the ASR gels was extended to 24 h, which is 3.4 times the control group. By incorporating aluminum, the initial moisture absorption at 10 and 30 min was significantly mitigated. The 1-h intensity of the two peaks is 70.8 % and 76.6 % lower than that of the control group, but 95.9 % and 49.0 % higher than the lithium group, respectively. More considerable moisture absorption from 1 to 4 h was observed from the aluminum group, and the moisture equilibrium was reached at 12 h, which is 5 h slower than the control group. While lithium exhibits a more efficient role than aluminum in modifying the moisture absorption rate of ASR gel, the final equilibrium amount of moisture at 48 h was not

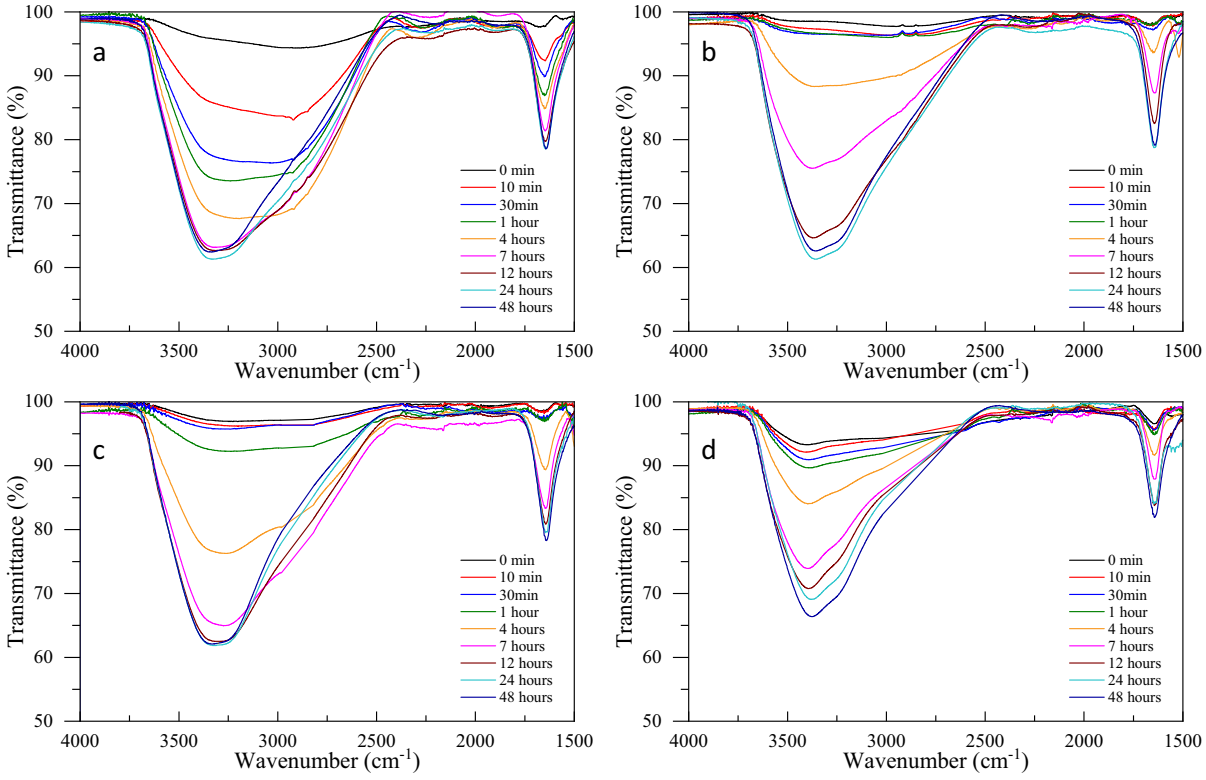

Fig. 16. ATR-FTIR spectra of (a) control ASR gel and ASR gels containing (b) lithium, (c) aluminum, and (d) combined lithium and aluminum exposed to 97 % RH over time.

considerably changed in the presence of lithium and aluminum.

Interestingly, the ASR gel containing coupled lithium and aluminum showed more initial water than the control at 0 h before the exposure to 97 % RH, which is in agreement with the TGA results. The moisture uptake of the ASR gel during the first 10 min and 20 min is considerably mitigated in the presence of the coupled lithium and aluminum, which the efficiency is lower than that of single lithium and aluminum. After 1 h, the ASR gel containing both lithium and aluminum absorbed 59.5 % and 23.9 % more water than the lithium-bearing and aluminum-bearing ASR gels, respectively. The synergistic effect between lithium and aluminum was observed from 4 h, where the increased amplitude over time is significantly suppressed. After 48 h, the intensity of the two peaks at 3690 cm^{-1}–2400 cm^{-1} and ~1640 cm^{-1} are about 11 % and 7 % lower than the other three groups. This synergistic effect between lithium and aluminum agrees well with the most effective ASR expansion mitigation and permeability improvement in the mortars.

3.6.3.2. Dynamic vapor sorption analysis. The influences of lithium, aluminum, and their coexistence on dynamic vapor adsorption and desorption behavior of ASR gels under varying RH are shown in Fig. 17a. The control sample took around 171 h to complete a "desorption-adsorption" cycle, while the ASR gels containing lithium and aluminum need 0.6 and 3.2 more hours, respectively, which is in agreement with the extended equilibrium time obtained at 97 % RH (see Fig. 16). The co-existence of lithium and aluminum, however, resulted in a decreased cycle time. Moreover, the control group showed an incredible water absorption of 200 % at 95 % RH, while in the presence of lithium and aluminum, the water absorption at the same RH decreased by 26 % and 52 %, respectively. The lowest water absorption of 135 % at 95 % RH was obtained from the sample coupled with lithium and aluminum, indicating its most effective role in reducing the water absorption of ASR products.

Fig. 17b shows the DVS isotherms of the control ASR gel and the ASR gels containing lithium, aluminum, and coupled lithium and aluminum. According to the International Union of Pure and Applied Chemistry (IUPAC) classification [99], there exist five types of sorption isotherms: the Langmuir adsorption isotherm (type I) commonly observed from microporous solids with a relatively small external surface, the S-shaped or sigmoid isotherm (type II) for non-porous or microporous adsorbents with unrestricted monolayer-multilayer adsorption, the convex isotherm (type III) in which the adsorbent-absorbate interactions at different RH play an important role, the isotherm with hysteresis loop attributed to the filling/vacating of mesopores by capillary condensation (Type IV), the S-shaped isotherm with hysteresis loop (Type V) related to the Type III isotherm with a weak adsorbent-adsorbate interaction, and the stepped isotherm (Type VI) for stepwise multilayer adsorption on a uniform non-porous surface. For the control group, the sorption isotherm is in line with the Type III isotherm pattern with limited hysteresis, which is only up to 2.3 % for the RH between 0 % and 80 %. In this case, the uptake curve is convex to the RH. At low RH, the moisture molecules are clustered around the most favorable sites on the surface with a relatively weak adsorbent-adsorbate interaction, while the uptake exhibits a sharp increase at an RH higher than 80 %. By adding lithium, aluminum, and their combination, the sorption curves were changed to a pattern similar to Type II and Type IV isotherms, where a gradual curvature with turning points B as an indication of the completion of monolayer coverage by moisture molecules and the beginning of multilayer absorption, as well as a Type H4 hysteresis loops in the middle section of the isotherms [100] were observed. The less distinctive point B in the isotherm of the control group indicates a significant amount of overlap of monolayer coverage and the onset of multilayer adsorption, which might be due to the low absorbent-absorbate interplay at low RH. The more significant hysteresis observed in a middle RH range between 10 % and 80 % from the ASR gels containing lithium and aluminum indicates a more capillary condensation in the multilayer range of moisture uptake due to the adsorption metastability in the open "ink-bottle" pores, which consist of a narrow pore entry (neck) and a wide interior part (cavity) [101]. The intrusion of water molecules into the inner cavity occurs when sufficient pressure is yielded in the narrow entries, while the desorption process follows the formation of a hemispherical meniscus in the narrow necks acting as a pore blocker to obstruct the emptiness of the cavity. This further indicates the modification of the pore structure of ASR gels in the presence of lithium and aluminum so that less moisture absorption and more effective pressure release can be obtained, making the ASR gel less destructive.

3.6.3.3. Water uptake capacity. The water uptake capacity of the studied ASR gels was determined in terms of equilibrium moisture content under the saturated surface dry condition (SSD) via DVS. Fig. 18a shows the mass drop of the wetted ASR gels during the drying process at 40 % RH and 40 °C. It can be seen that the control ASR gel reached equilibrium after around 370 min with a 47 % mass loss. In the presence of lithium and aluminum, the time for the ASR gels reaching equilibrium was shortened to 145 min and 200 min, with mass losses of 45.5 % and 48 %, respectively. The co-existence of lithium and aluminum shortened

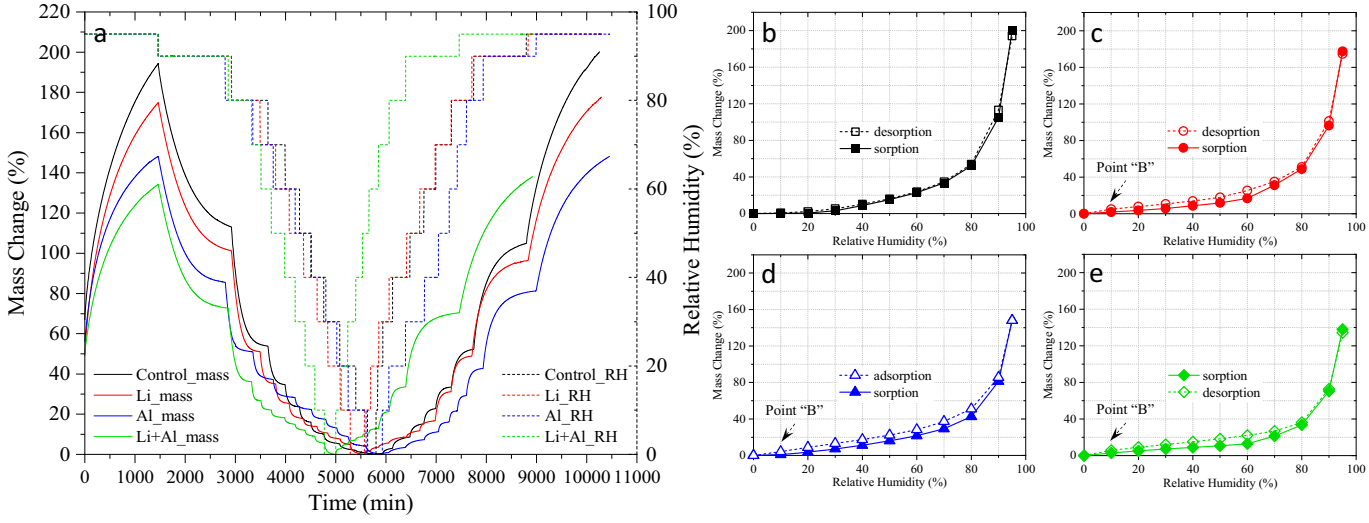

Fig. 17. (a) Drying and wetting curves and equilibrium moisture profiles of the ASR gels and isotherms of (b) control, (c) lithium, (d) aluminum, and (e) coupled lithium and aluminum-bearing ASR gels.

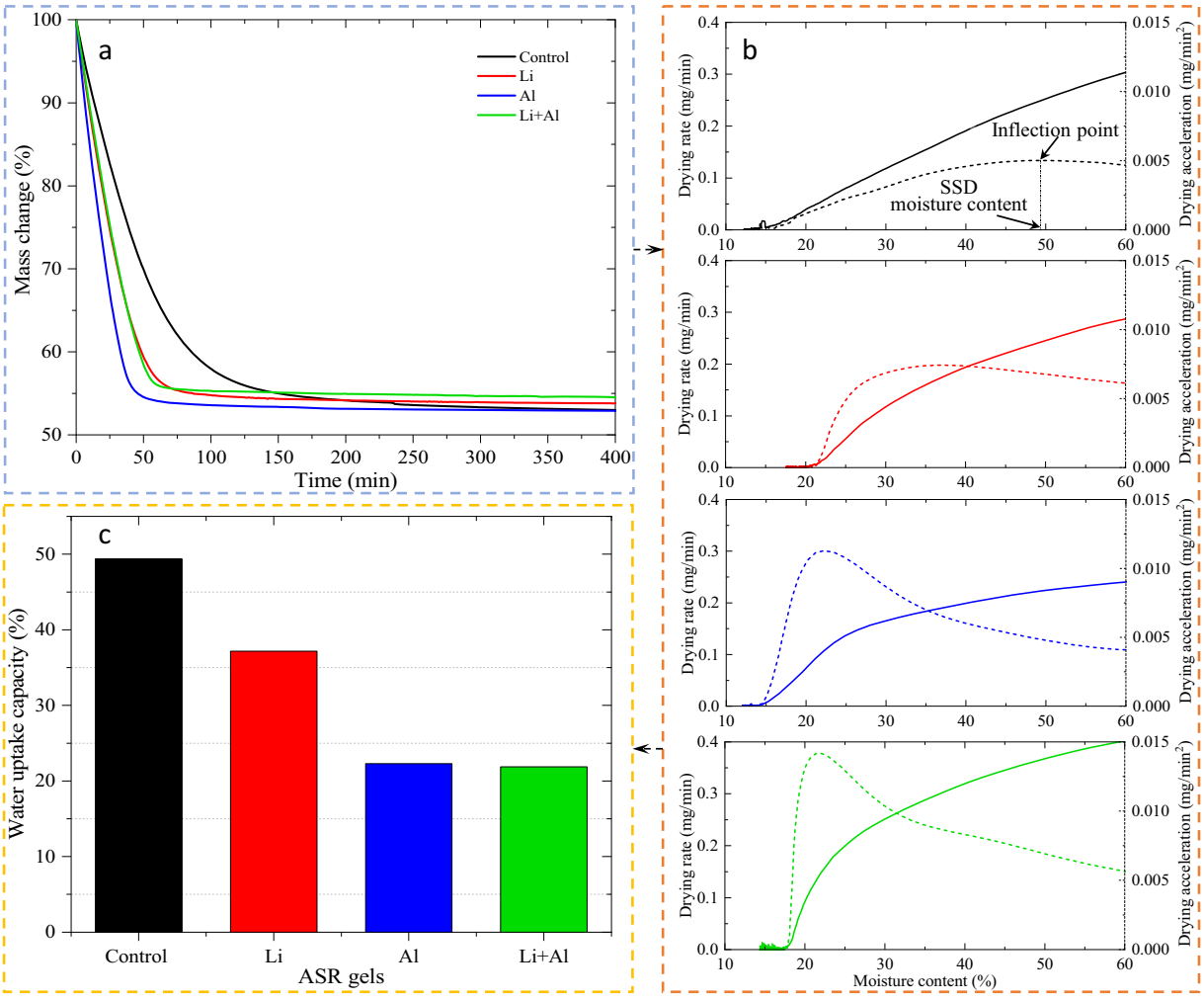

Fig. 18. (a) Mass change curves drying from wet to equilibrium at 40 % RH and 40 °C, (b) drying rate (solid) and drying acceleration (dash) curves, and (c) the water uptake capacity to reach SSD condition of the control ASR gel and the ASR gels containing lithium, aluminum, and their combination.

the drying time by 65.5 %, with a 44.6 % mass loss. These observations indicate the effective role of lithium and aluminum in decreasing the water uptake capacity of the ASR gel. Fig. 18b presents the drying rate and drying acceleration curves of four ASR gels derived from their mass change curves. By extracting the inflection points corresponding to the SSD moisture contents, the water uptake capacity of the ASR gels from dry condition to SSD was determined. As shown in Fig. 18c, the control ASR gel shows a water uptake capacity of 49.4 %, while it decreased to 37.2 % when lithium was added to the gel. A more pronounced water uptake capacity was yielded with the aluminum addition, which is 60.4 % lower than that of the control gel. The most effective decrease in water uptake capacity was obtained when lithium and aluminum were added simultaneously, which is 44.3 % of the control group. Thus, the decreased water uptake capacity of the ASR gels might be one possible reason for the most mitigated expansion obtained from the lithium and MK samples in the mortar bar test (see Fig. 3).

3.6.4. Suppression of free swelling behavior of ASR gels

Fig. 19 displays the volume change of the ASR gels after exposure to the simulated pore solution for up to 72 days. The significant and continuous swelling of the control ASR gel was observed, which yielded a 1.1 % expansion at 72 days. By adding lithium at a Li/[K + Na] ratio of 0.3, no expansion but a shrinkage was obtained. As a result, the volume of the ASR gel was decreased by 0.43 % at 16 days. Thereafter, a slight swelling was observed, and the total volume shrinkage was decreased to 0.35 % at 72 days. It should be noted that, due to the extreme slow

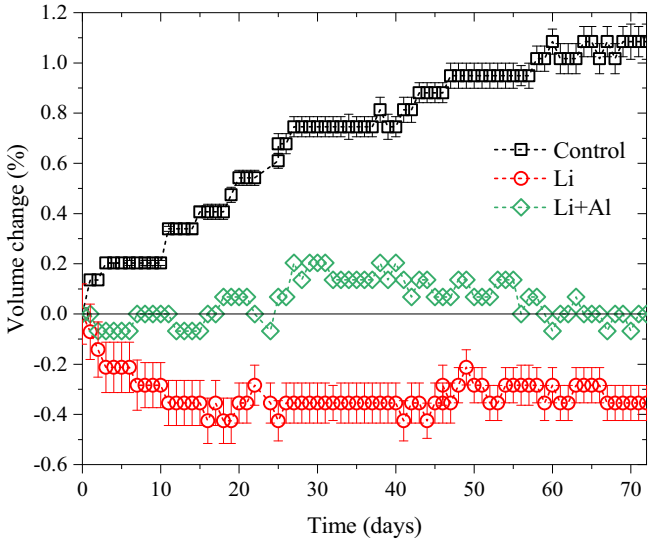

Fig. 19. Volume change of ASR gels exposed to pore solution.

hardening and high shrinkage of the ASR gel containing aluminum, its swelling behavior was not able to be measured via the proposed procedure, while this provides an indication that the incorporation of aluminum enables the conversion of ASR gel to a less expansive product. Interestingly, no significant volume change was observed from the ASR gel containing both lithium and aluminum, in which only an oscillation between −0.07 % and 0.14 % was exhibited. Thus, the side-effect of lithium (i.e., shrinkage) was compensated by aluminum. Moreover, this enhanced volume stability indicates the favorable role of the coupled lithium and aluminum in mitigating ASR-induced deterioration in concrete.

4. Conclusions

In this study, the role of a novel metakaolin-based internal conditioning (MIC) based on pre-wetted metakaolin with varying degrees of saturation (DOS) in alkali-silica reaction (ASR) suppression has been explored. The efficiency of MIC with and without lithium in mitigating ASR-induced volume expansion, cracking, permeability, strength loss, and microstructure evolution of mortars containing highly reactive aggregates was evaluated. To gain a comprehensive insight on the mitigation mechanisms, the influences of aluminum, lithium and their combination on multiple prerequisites of ASR deterioration, including silica dissolution, phase evolution, static and dynamic moisture uptake, and swelling behavior of synthetic ASR gels, were evaluated using inductively coupled plasma optical emission spectrometry, thermal gravimetry, X-ray diffraction, attenuated total reflection-Fourier transforms infrared spectroscopy, dynamic vapor sorption analysis, and a novel hygroscopic swelling measurement. Based on the experimental results and discussion, the following conclusions can be drawn:

1. Compared with lithium, the incorporation of 30 wt% MK exhibited a more effective role in suppressing ASR-induced volume expansion. While dry MK showed higher efficiency in decreasing early-age expansion, the long-term ASR expansion decreased with the DOS of MK, indicating the benefit of MIC in enhancing the ASR suppression efficiency of MK.
2. Agreeing with the suppressed ASR expansion, MIC led to more significant decreases in the average and maximum crack widths, as well as cracking density, than lithium. The microstructure analysis indicated the formation of microcracks in plain mortar inside both aggregate and the cement matrix filled with amorphous ASR gels with an average Ca/Si ratio of 0.46, while no cracks with ASR gels can be detected from the MIC groups.
3. Due to the introduction of the high amount of water and Li^+, although the ASR was effectively mitigated, the groups with MIC or lithium showed comparable bulk resistivity and formation factors with the plain mortar, which is lower than that of the mortar with dry MK. Despite the lower early-age strength under regular curing, a sustained strength gain was observed from the MIC group even after being transferred to the hot-alkaline accelerated aging condition, which highlighted the effective ASR mitigation.
4. The coupled incorporation of saturated MK and lithium exhibited higher efficiency outperforming the single uses of lithium or MK in suppressing expansion, reducing cracking density, densifying microstructure, decreasing permeability, and improving ultimate strength, which all indicated the synergistic effects between lithium and saturated MK (LiMIC) in mitigating ASR.
5. Lithium and aluminum play different roles in mitigating silica dissolution, where lithium can increase the initial silicon concentration during the first 24 h but showed high efficiency in mitigating silica dissolution at later ages, while a reversed phenomenon was observed from aluminum, which effectively mitigated silica dissolution during the first 168 h. These findings explain the optimum ASR mitigation from the LiMIC group, where lithium and aluminum synergize to decrease the silica dissolution at both early and later ages.
6. The synthetic ASR gel with Ca/Si, K/Si, and Na/Si ratios of 0.5, 0.2, and 0.8, respectively, showed the formations of ASR-related phases (i.e., tobermorite, fedorite, and Q^3 phase), the amounts of which increased with time. In contrast, in the ASR gels containing lithium and aluminum, fewer ASR gels were formed, and the conversion of the expansive ASR (Q^3) gels into non-expansive C-S-H (Q^2) phases was observed. As a result, the ASR gel's static moisture absorption under constant 97 % relative humidity, dynamic vapor sorption capacity under varying RH between 0 % and 95 %, as well as water uptake to reach the saturated surface dry condition were all suppressed.
7. An extraordinary hygroscopic expansion of 1.1 % was yielded by the synthetic ASR gel after exposure to a simulated pore solution for 72 days. Yet, shrinkage of up to 0.35 % was observed from the ASR gel containing lithium (Li/[K + Na] ratio of 0.3). By adding both lithium and aluminum at a Li/[K + Na] ratio of 0.3 and Al/Si ratio of 0.3, no significant volume change could be detected from the ASR gel explaining the robust ASR mitigation efficiency.

CRediT authorship contribution statement

Dayou Luo: Investigation, Validation, Formal analysis, Writing – original draft. **Arkabrata Sinha:** Investigation, Formal analysis, Writing – original draft. **Madhab Adhikari:** Investigation. **Jianqiang Wei:** Conceptualization, Methodology, Data curation, Supervision, Writing – review & editing, Project administration, Funding acquisition.

Declaration of competing interest

The authors declare that they have no known competing financial interests or personal relationships that could have appeared to influence the work reported in this paper.

Acknowledgment

This work was supported by the United States National Science Foundation (NSF) under the award No. 1935799. The authors gratefully acknowledge the support from this funding. The findings presented herein are those of the authors and do not necessarily reflect the views of the sponsor.

References

[1] T.E. Stanton, Influence of cement and aggregate on concrete expansion, in: Eng. News-Rec, 1940.
[2] J. Wei, B. Gencturk, A. Jain, M. Hanifehzadeh, Mitigating alkali-silica reaction induced concrete degradation through cement substitution by metakaolin and bentonite, Appl. Clay Sci. 182 (2019), 105257, https://doi.org/10.1016/j.clay.2019.105257.
[3] F. Rajabipour, E. Giannini, C. Dunant, J.H. Ideker, M.D. Thomas, Alkali–silica reaction: current understanding of the reaction mechanisms and the knowledge gaps, Cem. Concr. Res. 76 (2015) 130–146, https://doi.org/10.1016/j.cemconres.2015.05.024.
[4] R.-P. Martin, O.O. Metalssi, F. Toutlemonde, Importance of considering the coupling between transfer properties, alkali leaching and expansion in the modelling of concrete beams affected by internal swelling reactions, Constr. Build. Mater. 49 (2013) 23–30, https://doi.org/10.1016/j.conbuildmat.2013.08.008.
[5] F. Gong, Y. Takahashi, I. Segawa, K. Maekawa, Mechanical properties of concrete with smeared cracking by alkali-silica reaction and freeze-thaw cycles, Cem. Concr. Compos. 111 (2020), 103623, https://doi.org/10.1016/j.cemconcomp.2020.103623.
[6] T. Ueda, J. Kushida, M. Tsukagoshi, A. Nanasawa, Influence of temperature on electrochemical remedial measures and complex deterioration due to chloride attack and ASR, Constr. Build. Mater. 67 (2014) 81–87, https://doi.org/10.1016/j.conbuildmat.2013.10.020.
[7] R. Swamy, M. Al-Asali, Engineering properties of concrete affected by alkali-silica reaction, ACI Mater. J. 85 (1988) 367–374.
[8] S.M. Shafaatian, A. Akhavan, H. Maraghechi, F. Rajabipour, How does fly ash mitigate alkali–silica reaction (ASR) in accelerated mortar bar test (ASTM

C1567)? Cem. Concr. Compos. 37 (2013) 143–153, https://doi.org/10.1016/j.cemconcomp.2012.11.004.
[9] M. Thomas, F. Innis, Effect of slag on expansion due to alkali aggregate reaction in concrete, ACI Mater. J. 95 (1998) 716–724.
[10] M.H. Shehata, M.D. Thomas, Use of ternary blends containing silica fume and fly ash to suppress expansion due to alkali–silica reaction in concrete, Cem. Concr. Res. 32 (2002) 341–349, https://doi.org/10.1016/S0008-8846(01)00680-9.
[11] F. Bektas, K. Wang, Performance of ground clay brick in ASR-affected concrete: effects on expansion, mechanical properties and ASR gel chemistry, Cem. Concr. Compos. 34 (2012) 273–278, https://doi.org/10.1016/j.cemconcomp.2011.09.012.
[12] M.J. Munir, S.M.S. Kazmi, A. Khitab, M. Hassan, Utilization of rice husk ash to mitigate alkali silica reaction in concrete, in: Proceedings of 2nd International Multi-disciplinary Conference, University of Lahore, Gujrat Campus, Pakistan, 2016, p. 20.
[13] A. Trümer, H.-M. Ludwig, Sulphate and ASR resistance of concrete made with calcined clay blended cements, in: Calcined Clays for Sustainable Concrete, Springer, 2015, pp. 3–9.
[14] J. Lumley, ASR suppression by lithium compounds, Cem. Concr. Res. 27 (1997) 235–244, https://doi.org/10.1016/S0008-8846(97)00003-3.
[15] K. Folliard, M. Thomas, K. Kurtis, Guidelines for the Use of Lithium to Mitigate or Prevent ASR, 2003.
[16] W. McCoy, A. Caldwell, New approach to inhibiting alkali-aggregate expansion, J. Proc. (1951) 693–706.
[17] M. Lawrence, H. Vivian, Reactions of various alkalis with silica, Aust. J. Appl. Sci. 12 (1961) 96–103. http://hdl.handle.net/102.100.100/331477?index=1.
[18] S. Diamond, Unique response of LiNO3 as an alkali silica reaction-preventive admixture, Cem. Concr. Res. 29 (1999) 1271–1275, https://doi.org/10.1016/S0008-8846(99)00115-5.
[19] C. Tremblay, M. Bérubé, B. Fournier, M. Thomas, K.J. Folliard, Experimental investigation of the mechanisms by which LiNO3 is effective against ASR, Cem. Concr. Res. 40 (2010) 583–597, https://doi.org/10.1016/j.cemconres.2009.09.022.
[20] A. Leemann, L. Lörtscher, L. Bernard, G. Le Saout, B. Lothenbach, R.M. Espinosa-Marzal, Mitigation of ASR by the use of LiNO3—characterization of the reaction products, Cem. Concr. Res. 59 (2014) 73–86, https://doi.org/10.1016/j.cemconres.2014.02.003.
[21] S. Guo, Q. Dai, R. Si, Effect of calcium and lithium on alkali-silica reaction kinetics and phase development, Cem. Concr. Res. 115 (2019) 220–229, https://doi.org/10.1016/j.cemconres.2018.10.007.
[22] M.J. Millard, K.E. Kurtis, Effects of lithium nitrate admixture on early-age cement hydration, Cem. Concr. Res. 38 (2008) 500–510, https://doi.org/10.1016/j.cemconres.2007.11.009.
[23] L. Chen, L. Wang, D.-W. Cho, D.C. Tsang, L. Tong, Y. Zhou, J. Yang, Q. Hu, C. S. Poon, Sustainable stabilization/solidification of municipal solid waste incinerator fly ash by incorporation of green materials, J. Clean. Prod. 222 (2019) 335–343, https://doi.org/10.1016/j.jclepro.2019.03.057.
[24] T. Yang, Q. Wu, H. Zhu, Z. Zhang, Geopolymer with improved thermal stability by incorporating high-magnesium nickel slag, Constr. Build. Mater. 155 (2017) 475–484, https://doi.org/10.1016/j.conbuildmat.2017.08.081.
[25] G. Kaladharan, T. Szeles, S.M. Stoffels, F. Rajabipour, Novel admixtures for mitigation of alkali-silica reaction in concrete, Cem. Concr. Compos. 120 (2021), 104028, https://doi.org/10.1016/j.cemconcomp.2021.104028.
[26] A. Ramezanianpour, S.M.M. Karein, P. Vosoughi, A. Pilvar, S. Isapour, F. Moodi, Effects of calcined perlite powder as a SCM on the strength and permeability of concrete, Constr. Build. Mater. 66 (2014) 222–228, https://doi.org/10.1016/j.conbuildmat.2014.05.086.
[27] C. Ross, F. Davidson, E. Frankl, C. Meador, U. Kitzinger, E. Frankel, B. Bedenik, C. Besant, C. Calladine, J. Renton, Woodhead publishing series in civil and structural engineering, in: Rehabilitation of Pipelines Using Fiber-reinforced Polymer (FRP) Composites, Matthew Deans, 2016.
[28] M. Tapas, K. Vessalas, P. Thomas, V. Sirivivatnanon, P. Kidd, Mechanistic role of supplementary cementitious materials (SCMs) in alkali-silica reaction (ASR) mitigation, Concrete 2019: Concrete in practice-progress through knowledge: Proceedings of the Concrete Institute of Australia's Biennial National Conference, Sydney, Australia, 2019. September 8-11.
[29] T. Chappex, The Role of Aluminium From Supplementary Cementitious Materials in Controlling Alkali-Silica Reaction, 2012, https://doi.org/10.5075/epfl-thesis-5429.
[30] T. Ramlochan, M. Thomas, K.A. Gruber, The effect of metakaolin on alkali–silica reaction in concrete, Cem. Concr. Res. 30 (2000) 339–344, https://doi.org/10.1016/S0008-8846(99)00261-6.
[31] G.V. Walters, T.R. Jones, Effect of metakaolin on alkali-silica reaction (asr) in concrete manufactured with reactive aggregate, Spec. Publ. 126 (1991) 941–954.
[32] C. Bich, J. Ambroise, J. Péra, Influence of degree of dehydroxylation on the pozzolanic activity of metakaolin, Appl. Clay Sci. 44 (2009) 194–200, https://doi.org/10.1016/j.clay.2009.01.014.
[33] S. Wild, J.M. Khatib, A. Jones, Relative strength, pozzolanic activity and cement hydration in superplasticised metakaolin concrete, Cem. Concr. Res. 26 (1996) 1537–1544, https://doi.org/10.1016/0008-8846(96)00148-2.
[34] F. Wang, Y. Zhou, B. Peng, Z. Liu, S. Hu, Autogenous shrinkage of concrete with super-absorbent polymer, ACI Mater. J. 106 (2009) 123, https://doi.org/10.14359/56458.
[35] B. Craeye, M. Geirnaert, G. De Schutter, Super absorbing polymers as an internal curing agent for mitigation of early-age cracking of high-performance concrete bridge decks, Constr. Build. Mater. 25 (2011) 1–13, https://doi.org/10.1016/j.conbuildmat.2010.06.063.
[36] I. De la Varga, J. Castro, D. Bentz, J. Weiss, Application of internal curing for mixtures containing high volumes of fly ash, Cem. Concr. Compos. 34 (2012) 1001–1008, https://doi.org/10.1016/j.cemconcomp.2012.06.008.
[37] M.A. Beyene, J.F. Munoz, R.C. Meininger, C. Di Bella, Effect of internal curing as mitigation to minimize alkali-silica reaction damage, ACI Mater. J. 114 (2017), https://doi.org/10.14359/51689562.
[38] C. Li, M.D. Thomas, J.H. Ideker, A mechanistic study on mitigation of alkali-silica reaction by fine lightweight aggregates, Cem. Concr. Res. 104 (2018) 13–24, https://doi.org/10.1016/j.cemconres.2017.10.006.
[39] ASTMC150/C150M, Standard Specification for Portland Cement, 2021, https://doi.org/10.1520/C0150_C0150M-21.
[40] AASHTOM85, Standard Specification for Portland Cement, 2020.
[41] ASTMD281-12, Standard Test Method for Oil Absorption of Pigments by Spatula Rub-Out, 2021.
[42] B. Fournier, J.H. Ideker, K.J. Folliard, M.D. Thomas, P.-C. Nkinamubanzi, R. Chevrier, Effect of environmental conditions on expansion in concrete due to alkali–silica reaction (ASR), Mater. Charact. 60 (2009) 669–679, https://doi.org/10.1016/j.matchar.2008.12.018.
[43] L. Sanchez, T. Drimalas, B. Fournier, D. Mitchell, J. Bastien, Comprehensive damage assessment in concrete affected by different internal swelling reaction (ISR) mechanisms, Cem. Concr. Res. 107 (2018) 284–303, https://doi.org/10.1016/j.cemconres.2018.02.017.
[44] C. Trottier, R. Ziapour, A. Zahedi, L. Sanchez, F. Locati, Microscopic characterization of alkali-silica reaction (ASR) affected recycled concrete mixtures induced by reactive coarse and fine aggregates, Cem. Concr. Res. 144 (2021), 106426, https://doi.org/10.1016/j.cemconres.2021.106426.
[45] ASTMC1260, Standard Test Method for Potential Alkali Reactivity of Aggregates (Mortar-Bar Method), 2021, https://doi.org/10.1520/C1260-07.
[46] B. Lothenbach, Thermodynamic equilibrium calculations in cementitious systems, Mater. Struct. 43 (2010) 1413–1433, https://doi.org/10.1617/s11527-010-9592-x.
[47] T. Chappex, K.L. Scrivener, The influence of aluminium on the dissolution of amorphous silica and its relation to alkali silica reaction, Cem. Concr. Res. 42 (2012) 1645–1649, https://doi.org/10.1016/j.cemconres.2012.09.009.
[48] X. Hou, R.J. Kirkpatrick, L.J. Struble, P.J. Monteiro, Structural investigations of alkali silicate gels, J. Am. Ceram. Soc. 88 (2005) 943–949, https://doi.org/10.1111/j.1551-2916.2005.00145.x.
[49] Y. Luo, S. Li, K. Klima, H. Brouwers, Q. Yu, Degradation mechanism of hybrid fly ash/slag based geopolymers exposed to elevated temperatures, Cem. Concr. Res. 151 (2022), 106649, https://doi.org/10.1016/j.cemconres.2021.106649.
[50] A. Attar, B. Gencturk, H. Aryan, J. Wei, Impact of laboratory-accelerated aging methods to study alkali–silica reaction and reinforcement corrosion on the properties of concrete, Materials 13 (2020) 3273, https://doi.org/10.3390/ma13153273.
[51] ASTMC1876-19, Standard Test Method for Bulk Electrical Resistivity or Bulk Conductivity of Concrete, ASTM International, 2019.
[52] C. Qiao, M.K. Moradllo, H. Hall, M.T. Ley, W.J. Weiss, Electrical resistivity and formation factor of air-entrained concrete, ACI Mater. J. 116 (2019) 85–93, https://doi.org/10.14359/51714506.
[53] C. Carrillo, J. Cidrás, E. Díaz-Dorado, A.F. Obando-Montaño, An approach to determine the weibull parameters for wind energy analysis: the case of Galicia (Spain), Energies 7 (2014) 2676–2700, https://doi.org/10.3390/en7042676.
[54] ASTMC1608, Standard Test Method for Chemical Shrinkage of Hydraulic Cement Paste, 2017, https://doi.org/10.1520/C1608-17.
[55] P. Virmani, Alkali-Silica Reaction Mechanisms and Detections: An Advanced Understanding, Federal Highway Administration, United States, 2014.
[56] K.J. Folliard, M.D. Thomas, B. Fournier, K.E. Kurtis, J.H. Ideker, Interim Recommendations for the Use of Lithium to Mitigate or Prevent Alkali-Silica Reaction (ASR), Federal Highway AdministrationOffice of Infrastructure Research and Development, United States, 2006.
[57] R. Figueira, R. Sousa, L. Coelho, M. Azenha, J. de Almeida, P. Jorge, C. Silva, Alkali-silica reaction in concrete: mechanisms, mitigation and test methods, Constr. Build. Mater. 222 (2019) 903–931, https://doi.org/10.1016/j.conbuildmat.2019.07.230.
[58] S. Wild, J. Khatib, Portlandite consumption in metakaolin cement pastes and mortars, Cem. Concr. Res. 27 (1997) 137–146, https://doi.org/10.1016/S0008-8846(96)00187-1.
[59] P. Azarsa, R. Gupta, Electrical resistivity of concrete for durability evaluation: a review, Adv. Mater. Sci. Eng. 2017 (2017), https://doi.org/10.1155/2017/8453095.
[60] O. Sengul, Use of electrical resistivity as an indicator for durability, Constr. Build. Mater. 73 (2014) 434–441, https://doi.org/10.1016/j.conbuildmat.2014.09.077.
[61] Y. Bu, J. Weiss, The influence of alkali content on the electrical resistivity and transport properties of cementitious materials, Cem. Concr. Compos. 51 (2014) 49–58, https://doi.org/10.1016/j.cemconcomp.2014.02.008.
[62] D. Koleva, O. Copuroglu, K. Van Breugel, G. Ye, J. De Wit, Electrical resistivity and microstructural properties of concrete materials in conditions of current flow, Cem. Concr. Compos. 30 (2008) 731–744, https://doi.org/10.1016/j.cemconcomp.2008.04.001.
[63] H. Whittington, J. McCarter, M. Forde, The conduction of electricity through concrete, Mag. Concr. Res. 33 (1981) 48–60, https://doi.org/10.1680/macr.1981.33.114.48.
[64] K.A. Snyder, X. Feng, B. Keen, T.O. Mason, Estimating the electrical conductivity of cement paste pore solutions from OH−, K+ and Na+ concentrations, Cem.

Concr. Res. 33 (2003) 793–798, https://doi.org/10.1016/S0008-8846(02)01068-2.
[65] A. Ramezanianpour, H.B. Jovein, Influence of metakaolin as supplementary cementing material on strength and durability of concretes, Constr. Build. Mater. 30 (2012) 470–479, https://doi.org/10.1016/j.conbuildmat.2011.12.050.
[66] J. Ambroise, S. Maximilien, J. Pera, Properties of metakaolin blended cements, Adv. Cem. Based Mater. 1 (1994) 161–168, https://doi.org/10.1016/1065-7355(94)90007-8.
[67] M.S. Islam, N. Ghafoori, Relation of ASR-induced expansion and compressive strength of concrete, Mater. Struct. 48 (2015) 4055–4066, https://doi.org/10.1617/s11527-014-0465-6.
[68] F. Lagier, K.E. Kurtis, Influence of Portland cement composition on early age reactions with metakaolin, Cem. Concr. Res. 37 (2007) 1411–1417, https://doi.org/10.1016/j.cemconres.2007.07.002.
[69] D.P. Bentz, W.J. Weiss, Internal Curing: A 2010 State-of-the-Art Review, US Department of Commerce,National Institute of Standards and Technology, 2011.
[70] A. Leemann, T. Katayama, I. Fernandes, M.A. Broekmans, Types of alkali–aggregate reactions and the products formed, Constr. Mater. 169 (2016) 128–135, https://doi.org/10.1680/jcoma.15.00059.
[71] A.G. Vayghan, F. Rajabipour, J.L. Rosenberger, Composition–rheology relationships in alkali–silica reaction gels and the impact on the gel's deleterious behavior, Cem. Concr. Res. 83 (2016) 45–56, https://doi.org/10.1016/j.cemconres.2016.01.011.
[72] I.G. Richardson, The nature of CSH in hardened cements, Cem. Concr. Res. 29 (1999) 1131–1147, https://doi.org/10.1016/S0008-8846(99)00168-4.
[73] T. Kim, J. Olek, Chemical sequence and kinetics of alkali-silica reaction part I. Experiments, J. Am. Ceram. Soc. 97 (2014) 2195–2203, https://doi.org/10.1111/jace.12992.
[74] X. Hou, L.J. Struble, R.J. Kirkpatrick, Formation of ASR gel and the roles of CSH and portlandite, Cem. Concr. Res. 34 (2004) 1683–1696, https://doi.org/10.1016/j.cemconres.2004.03.026.
[75] Z. Dai, T.T. Tran, J. Skibsted, Aluminum incorporation in the C-S–H phase of white Portland cement–metakaolin blends studied by 27 Al and 29 si MAS NMR spectroscopy, J. Am. Ceram. Soc. 97 (2014) 2662–2671, https://doi.org/10.1111/jace.13006.
[76] C. Love, I. Richardson, A. Brough, Composition and structure of C-S–H in white Portland cement–20% metakaolin pastes hydrated at 25 C, Cem. Concr. Res. 37 (2007) 109–117, https://doi.org/10.1016/j.cemconres.2006.11.012.
[77] X. Feng, M. Thomas, T. Bremner, K.J. Folliard, B. Fournier, Summary of research on the effect of LiNO3 on alkali–silica reaction in new concrete, Cem. Concr. Res. 40 (2010) 636–642, https://doi.org/10.1016/j.cemconres.2009.08.021.
[78] X. Feng, M. Thomas, T. Bremner, K.J. Folliard, B. Fournier, New observations on the mechanism of lithium nitrate against alkali silica reaction (ASR), Cem. Concr. Res. 40 (2010) 94–101, https://doi.org/10.1016/j.cemconres.2009.07.017.
[79] T. Oey, E.C. La Plante, G. Falzone, Y.-H. Hsiao, A. Wada, L. Monfardini, M. Bauchy, J.W. Bullard, G. Sant, Calcium nitrate: a chemical admixture to inhibit aggregate dissolution and mitigate expansion caused by alkali-silica reaction, Cem. Concr. Compos. (2020), 103592, https://doi.org/10.1016/j.cemconcomp.2020.103592.
[80] X. Feng, M. Thomas, T. Bremner, B. Balcom, K. Folliard, Studies on lithium salts to mitigate ASR-induced expansion in new concrete: a critical review, Cem. Concr. Res. 35 (2005) 1789–1796, https://doi.org/10.1016/j.cemconres.2004.10.013.
[81] Z. Shi, A. Leemann, D. Rentsch, B. Lothenbach, Synthesis of alkali-silica reaction product structurally identical to that formed in field concrete, Mater. Des. 190 (2020), 108562, https://doi.org/10.1016/j.matdes.2020.108562.
[82] Q. Guo, T. Wang, Study on preparation and thermal properties of sodium nitrate/silica composite as shape-stabilized phase change material, Thermochim. Acta 613 (2015) 66–70, https://doi.org/10.1016/j.tca.2015.05.023.
[83] D. Cruz, S. Bulbulian, E. Lima, H. Pfeiffer, Kinetic analysis of the thermal stability of lithium silicates (Li4SiO4 and Li2SiO3), J. Solid State Chem. 179 (2006) 909–916, https://doi.org/10.1016/j.jssc.2005.12.020.
[84] S. Barzgar, B. Lothenbach, M. Tarik, A. Di Giacomo, C. Ludwig, The effect of sodium hydroxide on Al uptake by calcium silicate hydrates (CSH), J. Colloid Interface Sci. 572 (2020) 246–256, https://doi.org/10.1016/j.jcis.2020.03.057.
[85] A. Leemann, L. Bernard, S. Alahrache, F. Winnefeld, ASR prevention—effect of aluminum and lithium ions on the reaction products, Cem. Concr. Res. 76 (2015) 192–201, https://doi.org/10.1016/j.cemconres.2015.06.002.
[86] L. Baingam, T. Nawa, E. Iwatsuki, T. Awamura, ASR formation of reactive chert in conducting model experiments at highly alkaline and temperature conditions, Constr. Build. Mater. 95 (2015) 820–831, https://doi.org/10.1016/j.conbuildmat.2015.07.179.
[87] G. Geng, Z. Shi, A. Leemann, C. Borca, T. Huthwelker, K. Glazyrin, I.V. Pekov, S. Churakov, B. Lothenbach, R. Dähn, Atomistic structure of alkali-silica reaction products refined from X-ray diffraction and micro X-ray absorption data, Cem. Concr. Res. 129 (2020), 105958, https://doi.org/10.1016/j.cemconres.2019.105958.
[88] E.F. Krivoshapkina, V.I. Mikhaylov, I.A. Perovskiy, M. Torlopov, Y.I. Ryabkov, P. V. Krivoshapkin, The effect of cellulose nanocrystals and pH value on the flotation process for extraction of minerals, J. Sol-Gel Sci. Technol. 92 (2019) 319–326, https://doi.org/10.1007/s10971-019-04983-8.
[89] X. Qu, Z. Zhao, X. Zhao, Microstructure and characterization of aluminum-incorporated calcium silicate hydrates (C–S–H) under hydrothermal conditions, RSC Adv. 8 (2018) 28198–28208, https://doi.org/10.1039/C8RA04423F.
[90] K.-J. Hünger, The contribution of quartz and the role of aluminum for understanding the AAR with greywacke, Cem. Concr. Res. 37 (2007) 1193–1205, https://doi.org/10.1016/j.cemconres.2007.05.009.
[91] R. Ylmén, U. Jäglid, B.-M. Steenari, I. Panas, Early hydration and setting of Portland cement monitored by IR, SEM and Vicat techniques, Cem. Concr. Res. 39 (2009) 433–439, https://doi.org/10.1016/j.cemconres.2009.01.017.
[92] D. Luo, J. Wei, Hydration kinetics and phase evolution of Portland cement composites containing sodium-montmorillonite functionalized with a non-ionic surfactant, Constr. Build. Mater. 333 (2022), 127386, https://doi.org/10.1016/j.conbuildmat.2022.127386.
[93] M. Król, P. Rożek, D. Chlebda, W. Mozgawa, Influence of alkali metal cations/type of activator on the structure of alkali-activated fly ash–ATR-FTIR studies, Spectrochim. Acta A 198 (2018) 33–37, https://doi.org/10.1016/j.saa.2018.02.067.
[94] J. Kim, R. Kitagaki, Behavior of hydrates in cement paste reacted with silicate-based impregnant, Cem. Concr. Compos. 114 (2020), 103810, https://doi.org/10.1016/j.cemconcomp.2020.103810.
[95] Z. Shi, G. Geng, A. Leemann, B. Lothenbach, Synthesis, characterization, and water uptake property of alkali-silica reaction products, Cem. Concr. Res. 121 (2019) 58–71, https://doi.org/10.1016/j.cemconres.2019.04.009.
[96] A. Fernández-Jiménez, A. Palomo, Mid-infrared spectroscopic studies of alkali-activated fly ash structure, Microporous Mesoporous Mater. 86 (2005) 207–214, https://doi.org/10.1016/j.micromeso.2005.05.057.
[97] A.S. de Vargas, D.C. Dal Molin, Â.B. Masuero, A.C. Vilela, J. Castro-Gomes, R. M. de Gutierrez, Strength development of alkali-activated fly ash produced with combined NaOH and Ca(OH)2 activators, Cem. Concr. Compos. 53 (2014) 341–349, https://doi.org/10.1016/j.cemconcomp.2014.06.012.
[98] Z. Deng, Utilization of lithium nitrate to mitigate alkali–silica reaction of architectural glass mortar: characteristics and mechanisms, Constr. Build. Mater. 315 (2022), 125433, https://doi.org/10.1016/j.conbuildmat.2021.125433.
[99] M. Thommes, K. Kaneko, A.V. Neimark, J.P. Olivier, F. Rodriguez-Reinoso, J. Rouquerol, K.S. Sing, Physisorption of gases, with special reference to the evaluation of surface area and pore size distribution (IUPAC Technical Report), Pure Appl. Chem. 87 (2015) 1051–1069, https://doi.org/10.1515/pac-2014-1117.
[100] K.S. Sing, Reporting physisorption data for gas/solid systems with special reference to the determination of surface area and porosity (Recommendations 1984), Pure Appl. Chem. 57 (1985) 603–619, https://doi.org/10.1351/pac198557040603.
[101] R.M. Espinosa, L. Franke, Inkbottle pore-method: prediction of hygroscopic water content in hardened cement paste at variable climatic conditions, Cem. Concr. Res. 36 (2006) 1954–1968, https://doi.org/10.1016/j.cemconres.2006.06.011.